



Numerical Analysis of the Influence of Trapezoidal Geometry in Phase Change Material Containers on Temperature Distribution in Concentrated Photovoltaic Panel Cooling

Korhan Ökten¹ · Mehmet Balta² · Burak Kurşun¹

Received: 12 March 2024 / Accepted: 18 August 2024
© King Fahd University of Petroleum & Minerals 2024

Abstract

In concentrated photovoltaic (PV) panels, the amount of waste heat generated increases due to the higher incident radiation on the panel surface, leading to a decrease in PV panel efficiency. Therefore, PV-PCM (Phase Change Material) integration is a widely used passive method to reduce and stabilize PV panel temperature. However, particularly in angled PV panels, the movement of the PCM within its container can cause uneven temperature distributions on the PV panel surface. To address this issue, this study employs a trapezoidal geometry to increase the amount of PCM and the surface area exposed to the environment in the regions where the molten PCM accumulates. Furthermore, the effects of PCM area and heat transfer coefficient to the environment on the temperature distribution of the PV panel for different trapezoidal geometries (different tilt angles and the ratio of side surfaces) were investigated. A numerical model was developed for these investigations, and this model was validated with experimental work found in the literature. The results showed that the surface temperature decreased by 5–21 K and the surface temperature uniformity improved between 10 and 44% depending on the parameter change with the use of trapezoidal geometry.

Keywords Phase change material · Photovoltaic panel · Trapezoidal geometry · Temperature distribution

List of Symbols

A	Cross-sectional area (mm ²)
A_{mush}	Mushy zone constant
CP	Specific heat capacity (J/kgK)
g	Gravitational acceleration 9.81 m ² /s
h	Enthalpy (kJ/kg)
h_{conv}	Heat transfer coefficient (W/m ² K)
H	Latent heat (J/kg)
K	Heat conduction (W/mK)
L	Latent heat of fusion (J/kg)
m	Mass (kg)
p	Pressure (Pa)
PCM	Phase change material

t	Time second
T	temperature (K)
TES	Thermal energy storage
u	x Component of velocity
v	y Component of velocity
V	Fluid velocity (m/s)
Q	Heat (W)
x	Liquid fraction

Greek Symbols

λ	Liquid fraction
β	Thermal expansion coefficient (1/K)
ρ	Density (kg/m ³)
μ	Dynamic viscosity (kg/ms)
ε	Small number
β	Angle (°)

✉ Korhan Ökten
korhan.okten@amasya.edu.tr

¹ Mechanical Engineering Department, Faculty of Engineering,
Amasya University, 05100 Amasya, Turkey

² Machinery and Metal Technologies Department, Technical
Sciences Vocational School, Amasya University, 05100
Amasya, Turkey



Subscripts and Superscripts

conv	Convection
fin	Final
<i>i</i>	Initial
<i>l</i>	Liquid
lat	Latent
<i>m</i>	Mean
<i>n</i>	Coefficient
pcm	Phase change material
ref	Reference
<i>s</i>	Solid
SBS	Side and bottom surfaces
sen	Sensible
sto	Storage
TS	Top surface
tot	Total
<i>w</i>	Wall
wind	Wind

1 Introduction

Solar panels are commonly used devices that transform solar energy into electrical energy. While these devices convert a portion of the absorbed energy into electricity, a significant portion remains as heat, elevating the temperature of the PV cells [1]. This effect is more pronounced in concentrated PV panels [2]. Elevated temperatures adversely affect the electricity production and efficiency of PV panels. Hence, controlling the PV panel temperature is crucial. Active and passive cooling systems are employed for this purpose. Active cooling typically involves fluid circulation to cool PV cells, necessitating additional energy for fluid movement. So, passive cooling systems have gained prominence. Among these, one extensively studied approach in the literature is the integration of PV-PCM (Phase Change Material)[3]. Through PV-PCM integration, the waste heat generated within the PV is absorbed at a constant temperature due to the solid–liquid phase change of the PCM [4].

The studies in the literature predominantly focus on enhancing the heat transfer between PV (photovoltaic) panels and PCM (phase change material). The primary hurdle in this pursuit lies in the thermal conductivity of the PCM. Therefore, researchers have directed their attention toward leveraging nanoparticles or fins to augment the thermal conductivity of PCM. [5, 6]. Nevertheless, incorporating extra components within the PCM container introduces cost and practical implementation challenges. Hence, it becomes crucial to ascertain the melting behavior of PCM within PV panels positioned at various angles. This effort aims to

resolve the heat transfer issue at the junction of PV-PCM. Abdulmunem et al. [7] examined the melting behavior of PCM and PV panel temperatures for panel angles of 0°, 30°, 60°, and 90°. The study revealed that the melting rate and cooling efficiency escalated as the panel angle increased from 0 to 90 degrees, attributed to enhanced convection effects. In the modeling carried out in this study, the combination of PV panels and PCM containers was modeled numerically. However, to shorten the calculation times, PCM melting characteristics have been examined in the literature by applying constant heat flux from the upper surface of the container [8]. Zennouhi et al. [9] investigated the melting behavior within the PCM container at various inclination angles. Correspondingly, as the inclination angle rose from 0 to 90°, there was an observed increase in the extent of melting. Abdulsanem et al. [10] studied the impact of various tilt angles on melting duration and cooling capability. The findings indicated that as the tilt angle increased, convection effects intensified, resulting in a reduction of melting time and an enhancement of cooling capacity. Liu et al. [11] rotated the rectangular PCM container around the heated surface and observed an increase in convection effects correlating with the rotation speed.

Increasing the tilt angle of PV-PCM integration significantly enhances cooling but hinders the uniform distribution of surface temperature across the panel. Emam and Ahmed [12] placed a PCM container with cavities beneath the PV panel to achieve temperature uniformity while reducing panel temperature. The study explored various configurations: single cavity, three parallel cavities, five parallel cavities, and three series cavities. Different PCMs were utilized within these cavities. The configuration that provided the lowest PV panel surface temperature and the most uniform temperature distribution was the one with five parallel cavities. Duan [13] used copper metal foam within the PCM container at the PV-PCM junction to mitigate convection effects and enhance the thermal conductivity of the PCM. The study investigated panel angle and foam density as variables. It was observed that the impact of the panel angle was significantly minimized using a porous PCM container, with the most favorable outcomes observed at 85% porosity.

Several studies in the literature focus on increasing the melting amount and, consequently, the heat extraction from the surfaces by employing various PCM container geometries. In the study by Manikandan et al. [14], simulations were conducted using vertical rectangular, horizontal rectangular, triangular, and cylindrical container geometries, all subjected to external heating during the drying process. The results indicated that horizontal rectangles provided the fastest melting and solidification times, while cylindrical shapes resulted in the longest durations for these processes. Additionally, incorporating fins significantly reduced melting and solidification times, with hollow fins offering advantages in material



efficiency, weight reduction, and cost savings. The study by Iachachene et al. [15] investigated the melting of a phase change material (PCM) placed in a trapezoidal cavity, heated on one side and cooled on the other. Initially, the cavity was filled with paraffin wax to examine the orientation effect on PCM performance, followed by the addition of graphene nanoparticles to evaluate the thermal performance of the nanofluid. The results indicated that both effects enhanced heat transfer, but the heat transfer performance of the NEPCM (Nano enhanced phase change material) was lower when the thermal conductivity enhancement was below 80%. In addition to these basic geometries, there are studies that utilize various alternative geometries. Liu et al. [16] propose a heptahedron energy storage unit designed to enhance natural convection. Three-dimensional numerical simulations have been conducted to investigate the effects of the heptahedron structure on the melting characteristics of RT42 phase change material (PCM). The results indicate that the heptahedron structure enhances natural convection, reduces the melting time of the PCM by 9.3%, and increases its average power by 8.47%. In addition to these studies, other research has primarily focused on increasing the melting amount by using nanoparticles or different fin geometries or placement [17–19]. The literature demonstrates that different container geometries can be utilized for various applications. Additionally, the number of studies examining PCM containers in the context of PV/PCM integration is quite limited. As is well known, the geometry of PCM containers in PV-PCM integrations is typically rectangular or square in cross section. However, in recent years, a limited number of studies have explored the application of trapezoidal geometries. Johrami et al. [20] examined the effects of combinations of trapezoidal, finned, and zigzag container geometries on PV panel temperature in vertically positioned PV panels. Ahmad et al. [21] have explored the container geometry by placing it on the base of the PV panel. This study examined the impact of a trapezoidal container geometry on panel temperature and found that employing this geometry positively contributed to cooling the PV panel. Within the study's scope, the contribution of different side lengths of the container and various PCMs on performance was investigated. However, these studies have not thoroughly examined how changes in the edge lengths of trapezoidal geometries, along with variations in PCM quantity and environmental conditions, affect the movement of PCM within the container. Consequently, the impact on PV surface temperature variations, uniformity, and heat storage capacity has not been explored in detail. Therefore, this study numerically investigates surface temperature, melting rate, melted PCM behavior (melting characteristics, velocity vectors and temperature distribution), heat storage capacity, and surface temperature uniformity in relation to the w_1/w_2 ratio, tilt angle, PCM area, and heat transfer coefficient (wind speed).

2 Model Description

In this section, detailed information about the physical model, numerical and mathematical model, and solution steps are given. First of all, the physical model is mentioned in Sect. 2.1.

2.1 Physical and Thermal Model

PV panels produce electricity with the effect of solar radiation. However, while some of the incoming energy is converted into electricity, an important part is turned into waste heat. Especially in CPV panels, the amount of waste heat is formed more. In PV/PCM integration, a significant part of this heat is transferred to the PCM container and the PV panel cools down significantly. In the PCM container, the liquid PCM in the lower zone moves upwards with the effect of natural convection, and the fluid temperature in the upper section of the PCM container begins to increase. This situation causes nonuniform temperature distribution in the PV module. Based on this heat transfer mechanism, the trapezoidal PCM container geometry shown in Fig. 1 is proposed in this study. In addition, in the created thermal model as seen in the figure, it is assumed that 1000 W/m^2 heat flux passes from the CPV to the PCM container. Therefore, a PCM container with a heat flux input from its upper surface was used as a model. Because the low and uniform PCM container surface temperature will positively affect the panel temperature and increased efficiency will be achieved. In addition, the computation time is significantly reduced with this model.

Within the scope of the study, different PCM container surface temperatures, PCM liquid fraction, and PCM temperature distributions were investigated in terms of ratios of the short side to the long side in trapezoidal geometry (w_1/w_2), PV tilt angle (β), heat transfer coefficient (h_{conv}), and PCM area (A_{PCM}). The same PCM area and heat transfer coefficient values were used in these examinations for both the basic and recommended models. As shown in Table 1, three basic geometries were determined as models during the analysis. The feature that distinguishes these models from each other is the w_1/w_2 ratio and for different w_1/w_2 ratios were evaluated for 30° , 45° and 60° panel tilt angles.

Finally, the trapezoidal model that the best results were obtained and Model 1 were compared for different heat transfer coefficients and PCM areas. For the examination, heat transfer coefficients were taken as $5.8 \text{ W/m}^2\text{K}$ ($V_{\text{wind}} = 1$), $8.8 \text{ W/m}^2\text{K}$ ($V_{\text{wind}} = 2$), and $11.8 \text{ W/m}^2\text{K}$ ($V_{\text{wind}} = 3$) $\text{W/m}^2\text{K}$, and PCM areas were taken as $0.8A$, $1A$ and $1.2A$ ($A = 1500 \text{ mm}^2$).



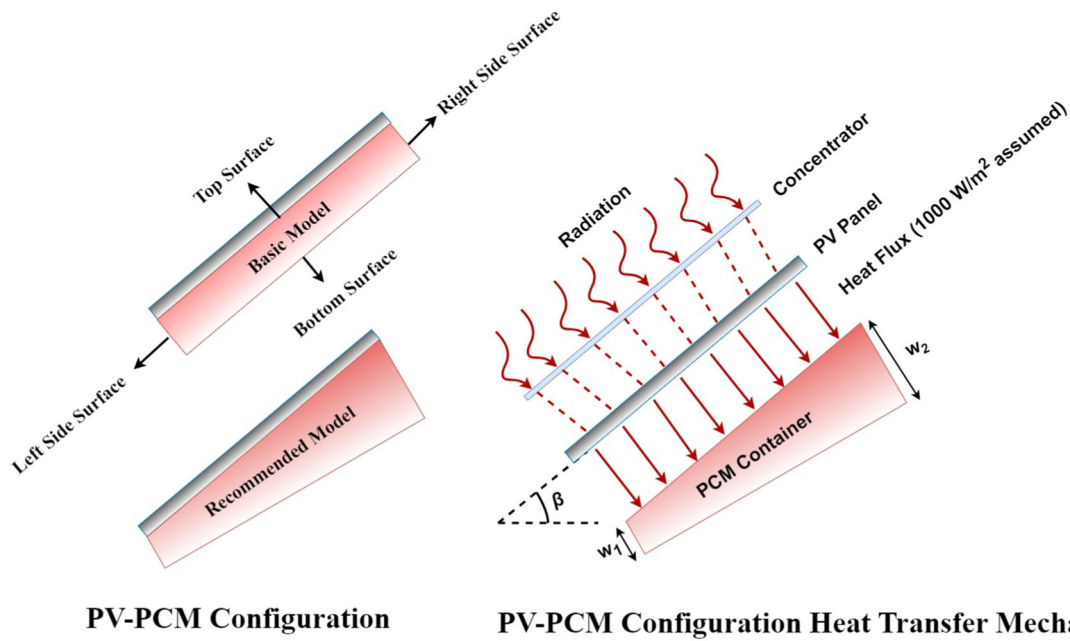


Fig. 1 System components and heat transfer mechanism

Table 1 PV/PCM models and variables

	w_1	w_2	w_1/w_2	β_1 (°)	β_2 (°)	β_3 (°)
Model 1	25	25	1	30	45	60
Model 2	15	35	2.33	30	45	60
Model 3	5	45	9	30	45	60

2.2 Mathematical Model

In the presented study, melting analysis of the phase change material was carried out. The enthalpy-porosity method was applied to solve the phase change numerically [22]. The following assumptions were used in the creation of the mathematical model.

- It was assumed that the flow was two-dimensional, incompressible, and Newtonian [23].
- The Boussinesq approach was preferred for natural convection flow. In the Boussinesq approach, it was assumed that the fluid density changes depending on the temperature. Other thermophysical properties of PCM were assumed to be constant [24].
- Viscous dissipation effect was ignored [25].
- The thermal expansion in the PCM container during melting was neglected [13].

The equations for the conservation of mass and energy are given as follows [26],

Continuity equation:

$$\frac{\partial \rho}{\partial t} + \frac{\partial(\rho u)}{\partial x} + \frac{\partial(\rho v)}{\partial y} = 0 \tag{1}$$

Momentum equation in x direction:

$$\frac{\partial(\rho u)}{\partial t} + \frac{\partial(\rho uu)}{\partial x} + \frac{\partial(\rho uv)}{\partial y} = -\frac{\partial p}{\partial x} + \frac{\partial}{\partial x} \left(\mu \frac{\partial u}{\partial x} \right) + \frac{\partial}{\partial y} \left(\mu \frac{\partial u}{\partial y} \right) + uA \tag{2}$$

Momentum equation in y direction:

$$\frac{\partial(\rho v)}{\partial t} + \frac{\partial(\rho uv)}{\partial x} + \frac{\partial(\rho vv)}{\partial y} = -\frac{\partial p}{\partial y} + \frac{\partial}{\partial x} \left(\mu \frac{\partial v}{\partial x} \right) + \frac{\partial}{\partial y} \left(\mu \frac{\partial v}{\partial y} \right) + vA + \rho g \beta (T - T_m) \tag{3}$$

where ρ represents the density, g represents the gravitational acceleration (9.81 m/s^2), μ represents the dynamic viscosity, β expresses the thermal expansion coefficient, T represents

the temperature, T_m represent melting temperature of PCM, and u and v denote the fluid velocities in the x and y directions, respectively. The Boussinesq approach is expressed with the last term in Eq. (3). The A number is found by Eq. (4) [23],

$$A = -A_{\text{mush}} \frac{(1 - \lambda)^2}{\lambda^3 + \varepsilon} \tag{4}$$

where λ denotes the liquid fraction and is defined by Eq. (5) [25],

$$\lambda = \begin{cases} 0; & T < T_s \\ (T - T_s)/(T_l - T_s); & T_s < T < T_l \\ 1; & T > T_l \end{cases} \tag{5}$$

where the subscripts l and s express the liquid state and the solid state, respectively. A_{mush} is the mushy zone constant and was taken as $A_{\text{mush}} = 10^6$ in this study. ε is the small number and was taken as $\varepsilon = 0.001$ [23].

The conservation of energy is defined by Eq. (6),

$$\frac{\partial(\rho h)}{\partial t} + \frac{\partial(\rho u h)}{\partial x} + \frac{\partial(\rho v h)}{\partial y} = \frac{\partial}{\partial x} \left(k \frac{\partial T}{\partial x} \right) + \frac{\partial}{\partial y} \left(k \frac{\partial T}{\partial y} \right) \tag{6}$$

where k is the thermal conductivity and, h is the sensible enthalpy. h is found with Eq. (7) [25],

$$h = \begin{cases} \int_{T_{\text{ref}}}^T c_p dT; & T < T_s \\ \int_{T_{\text{ref}}}^T c_p dT + \lambda H; & T_s < T < T_l \\ \int_{T_{\text{ref}}}^{T_s} c_p dT + \int_{T_l}^T c_p dT; & T > T_l \end{cases} \tag{7}$$

In the equations, c_p represents the specific heat capacity, H represents the latent heat and T_{ref} represents the reference temperature ($T_{\text{ref}} = 298.15$ K [27]). T is calculated by the following equation [28],

$$T = \lambda(T_l - T_s) + T_s \tag{8}$$

Finally, the thermal energy stored in the PCM container has been calculated. As is well known, the PCM container stores latent energy associated with melting the PCM and sensible heat related to the temperature increase. The calculations for sensible ($\dot{Q}_{\text{sen,sto}}$) and latent ($\dot{Q}_{\text{lat,sto}}$) energy storage are shown in Eqs. (9 and 10), respectively. In the equations, m_{PCM} represents the mass of the PCM, L_{PCM} is

Table 2 Thermophysical properties of lauric acid PCM [26]

Thermophysical properties	Value
Solidus/ Liquidus Temperature (K)	316.65
Liquid Density (kg/m ³)	885
Specific Heat Capacity (J/kgK)	2390
Latent Heat of Fusion (J/kg)	187,210
Thermal Conductivity (W/mK)	0.14
Thermal Expansion Coefficient (1/K)	0.0006
Dynamic Viscosity (kg/ms)	0.0059295

the latent heat of fusion, x_{PCM} is the liquid fraction, c_{PCM} is the specific heat of the PCM. $\bar{T}_{\text{in,PCM}}$ and $\bar{T}_{\text{fin,PCM}}$ denote the initial and final average temperatures of the PCM container, respectively.

$$\dot{Q}_{\text{lat,sto}} = m_{\text{PCM}} L_{\text{PCM}} x_{\text{PCM}} \tag{9}$$

$$\dot{Q}_{\text{sen,sto}} = m_{\text{PCM}} c_{\text{PCM}} (\bar{T}_{\text{in,PCM}} - \bar{T}_{\text{fin,PCM}}) \tag{10}$$

In Eq. (11), the total stored energy is calculated as the sum of Eqs. (9 and 10).

$$\dot{Q}_{\text{tot,sto}} = \dot{Q}_{\text{lat,sto}} + \dot{Q}_{\text{sen,sto}} \tag{11}$$

In the study, Lauric acid was preferred as a PCM because of suitable for energy storage applications at medium temperature levels. It also has features such as nontoxicity, good chemical stability [29]. The thermophysical properties of lauric acid are given in Table 2.

2.3 Boundary Conditions

The conservation equations of mass, momentum, and energy, as well as the boundary and initial conditions used for the analysis of the solution domain shown in Fig. 2, are as follows.

Boundary condition for outer (side and bottom) surface of aluminum PCM container:

$$\begin{aligned} -k \frac{\partial T}{\partial x} \Big|_{\text{SBS}} &= h_{\text{conv}}(T_w - T_{\text{amb}}), \quad t(s) \\ &= t; \quad h_{\text{conv}} = 2.8 + 3V_{\text{wind}} \end{aligned} \tag{12}$$

Boundary condition for top surface of PCM container:

$$-k \frac{\partial T}{\partial x} \Big|_{\text{TS}} = \dot{q}(1000 \text{ W/m}^2), \quad t(s) = t \tag{13}$$

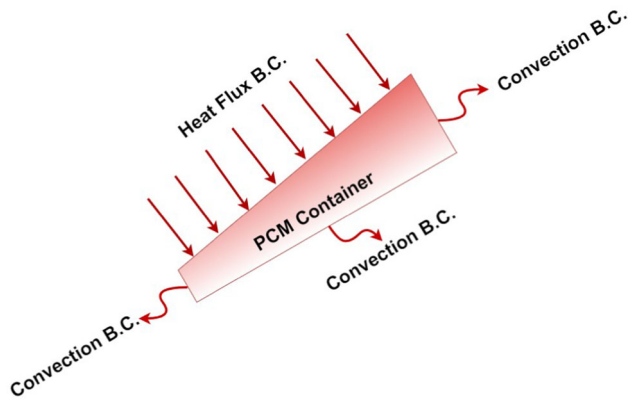


Fig. 2 Solution domain and boundary conditions

Initial condition:

$$T_{\text{PCM}} = 298.15 \text{ K}, \quad t(s) = 0 \quad (14)$$

In the equations, T_w is the wall temperature, T_{amb} is the mean fluid temperature, h_{conv} is the convection heat transfer coefficient, V_{wind} is the wind velocity, TS is the top surface and SBS is the side and bottom surface.

2.4 Numerical Method

The finite volume method was preferred in numerical analyses, and ANSYS 2022R1 software was used to apply the finite volume method. The PISO algorithm (Fig. 3) was used for the pressure–velocity coupling and the PRESTO! scheme was preferred for the pressure correction equation. The QUICK scheme was applied in the discretization of momentum and energy equations, and the first-order implicit transient formulation was used for the time-dependent solution of the equations [30]. Numerical analyzes were terminated when the residual values for each time step reached 10^{-4} for conservation of mass and velocity values and 10^{-8} for conservation of energy. An unstructured tetrahedral grid structure was applied to the computational domain.

The grid structures produced for PCM containers with rectangular and trapezoidal geometry are given in Fig. 4. Additionally, the numerical model's skewness and mesh quality values were approximately 0.94 and 7.3×10^{-2} , respectively.

3 Results and Discussion

In this section, the verification of the numerical model, the evaluation of w_1/w_2 and tilt angle (β), and the effects of the heat transfer coefficient (h_{conv}) and PCM area (A_{PCM}) were examined. The sequential steps illustrated in Fig. 5 were followed sequentially while conducting these examinations.

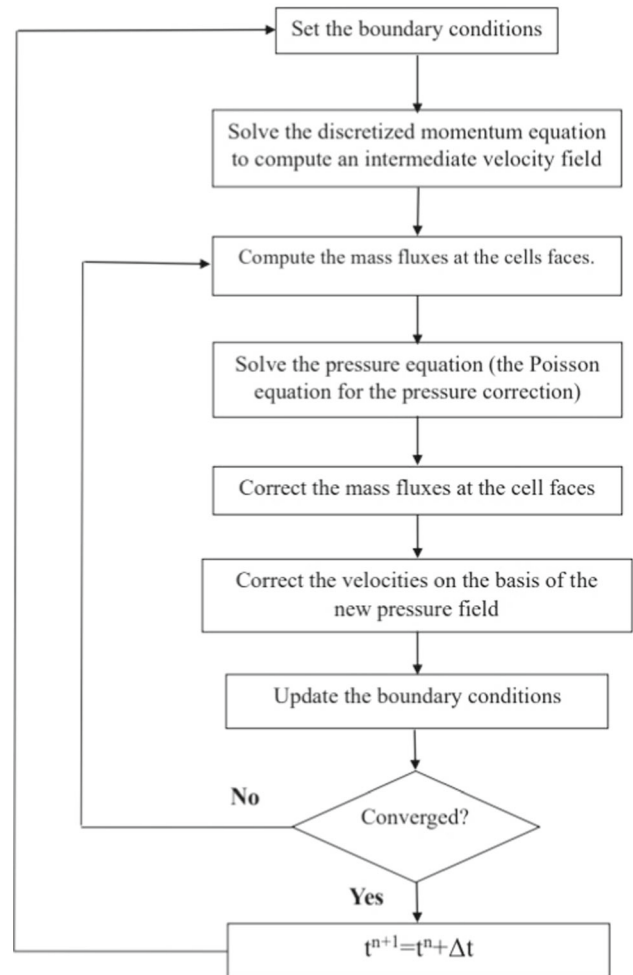


Fig. 3 PISO solution algorithm

3.1 Verification of Numerical Results

In numerical analysis, it is vital that the results are both accurate and performed using minimum computer power. Therefore, the optimum time step and grid number should be selected. For this purpose, the grid number and time step independence analyzes shown in Fig. 6 were performed. Figure 6a shows the liquid fraction change depending on the grid number. Since it was seen in the figure that there is a change of less than 1% of the liquid fraction value after the value of 12,200, the grid number was chosen as 12,200. In Fig. 4b, the liquid fraction change depending on the time step is seen. Similarly, since the values did not change significantly after 0.25 s, the time step value was taken as 0.25 s.

To demonstrate the accuracy of the numerical model, the obtained liquid fraction parameter was compared with the experimental study by Kamkari et al. [31]. Figure 7 presents a comparison of the time-dependent melting characteristics obtained experimentally and numerically (proposed numerical study). The results indicate that up to the 40th

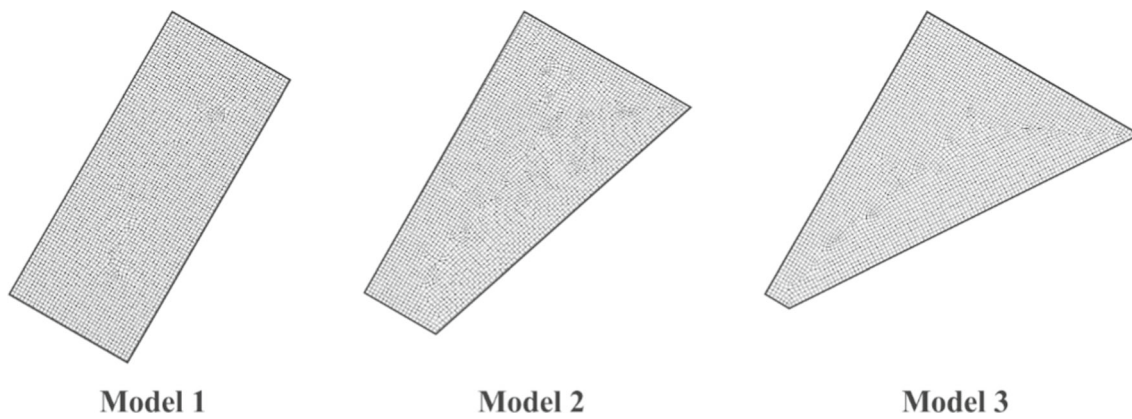


Fig. 4 Grid structures for rectangular and trapezoidal geometries (Model 1, Model 2 and Model 3)

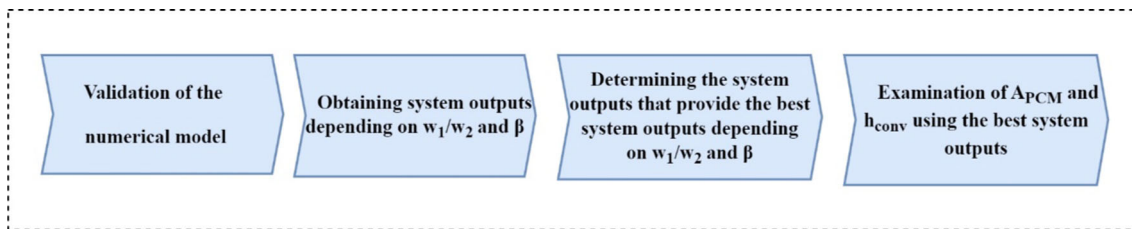


Fig. 5 Results examination steps

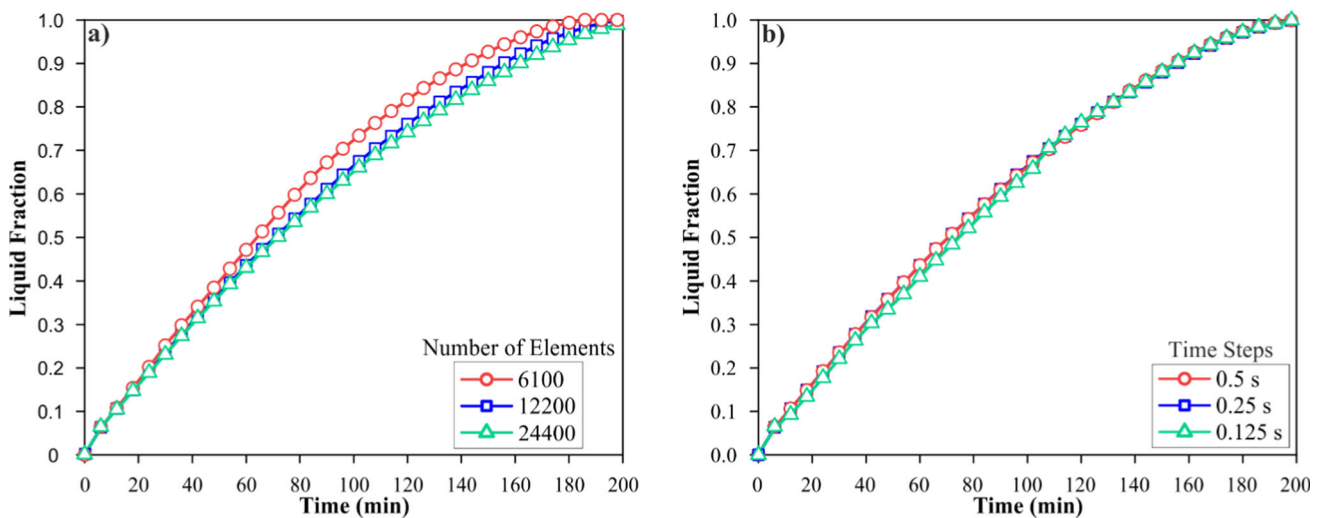


Fig. 6 a grid number b time step independence test results

minute, the melting characteristics of both experimental and numerical results are almost identical. After the 40th minute, although the melting rates remain similar, slight differences in the melting characteristics become apparent. These discrepancies are attributed to photographic deviations in the experimental study due to the increased melting rate, unpredictable solid–liquid (PCM) movements, and assumptions made in the numerical analysis.

As mentioned above, there are certain differences between experimental and numerical images; however, in the literature, the total melt amount in the container is generally used to demonstrate the accuracy of the numerical model. Therefore, Fig. 8 compares the experimental [31] and numerical [26] studies conducted by Kamkari et al. with the numerical study proposed in this paper in terms of liquid fraction. Upon reviewing the results, the experimental and numerical studies conducted in the literature are consistent with the proposed numerical study and exhibit similar characteristics. The

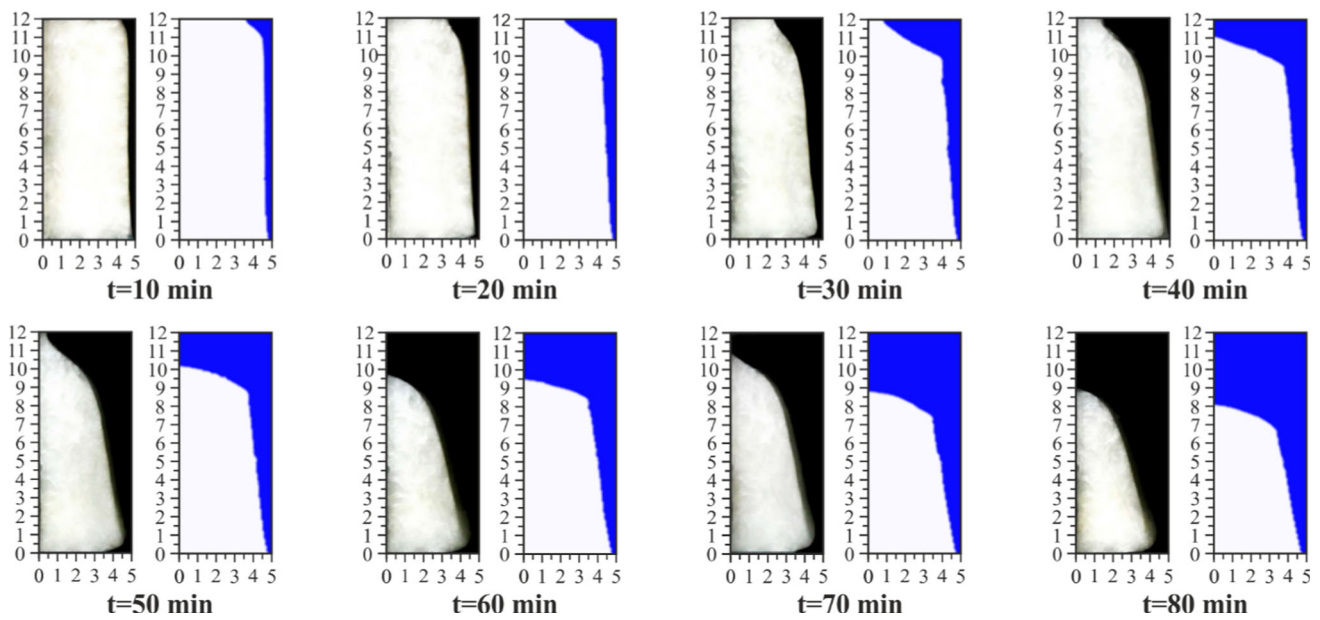


Fig. 7 Comparison of time-dependent liquid fraction of PCM for experimental [31] and numerical results

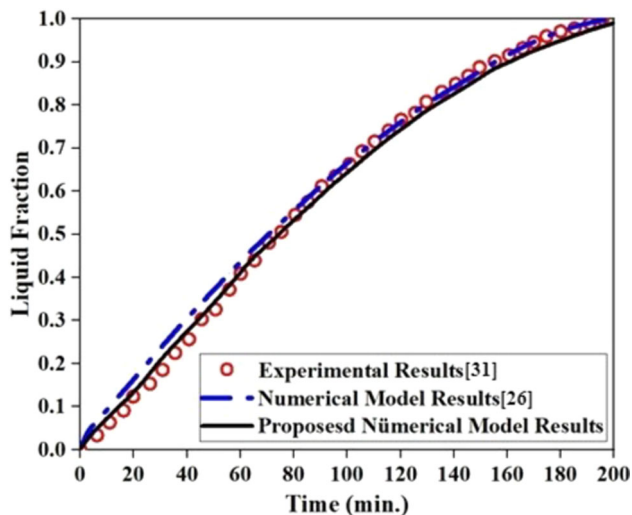


Fig. 8 PCM time-dependent liquid fraction verification

obtained data indicate that the proposed model exhibits an average deviation of approximately 1–5%, thereby demonstrating its usability.

3.2 The Evaluation of w_1/w_2 and Tilt Angle

In this section, the effects of the w_1/w_2 and tilt angle on average top surface temperature, liquid fraction, and melting characteristics were investigated. In the study, by choosing the trapezoidal geometry, the right-side surface of the PCM container was longer than the left side surface, thus more PCM area was obtained in the right-side part of the container. From this point of view, as a common feature in all

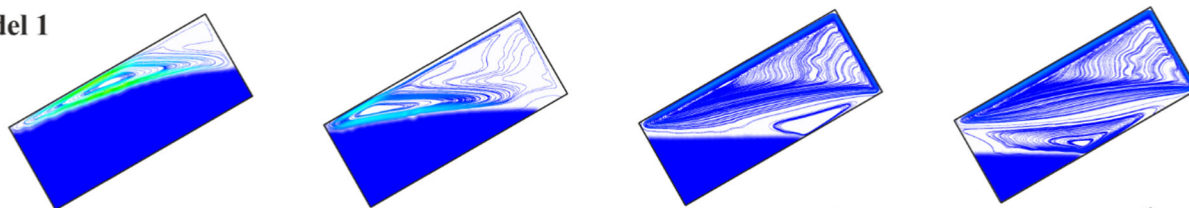
tilt angles (Fig. 9, 11, 13), the melted PCM moves toward the right part of the container by heating and lost a significant part of its heat to the solid PCM and the environment due to the trapezoidal geometry. Afterward, the liquid PCM, which loses its heat, will move toward the left side surface of the container again with the effect of gravity. During the movement of the container to the left side surface, the liquid PCM chose a direction closer to the bottom than the rectangular container, since it was cooled more with the use of trapezoidal geometry. This fluid movement showed that by increasing the right-side surface of the container, the liquid PCM transfers more heat to both the environment and the solid PCM. For this reason, both the container surface temperature decreased, and the liquid fraction increased.

Figure 9 shows the velocity vectors, temperature distribution, and melting characteristics of Model 1, Model 2, and Model 3 for 30° tilt angles. In 80 min for Model 1 and 120 min for Model 2, all the solid PCM in contact with the right-side surface was melted. In addition, it was seen that there is a more balanced melting in Model 3. This balanced melting characteristic ensures that heat can be transferred from the right part of the container to the solid PCM throughout the entire melting process for Model 3. However, in other models, overheating occurs over time, as there is a completely molten PCM on the right-side surface of the container. With this melting characteristic, although the average top surface temperature decreases slightly with the use of trapezoidal geometry, the effect of using trapezoidal geometry is limited since the convection effects are lower at 30° .

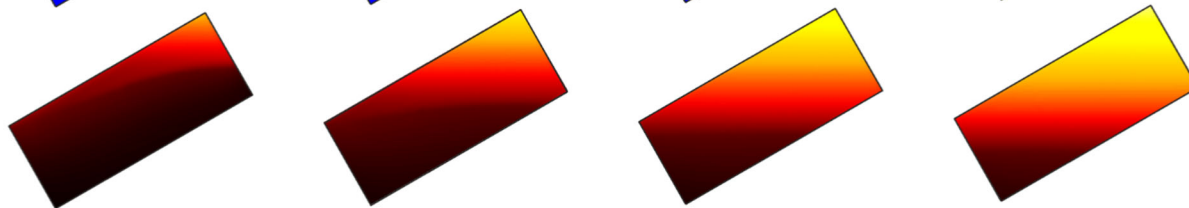
Figure 10 shows the time-dependent liquid fraction and PCM container average top surface temperatures for 30° tilt

Model 1

a)



b)



40 min

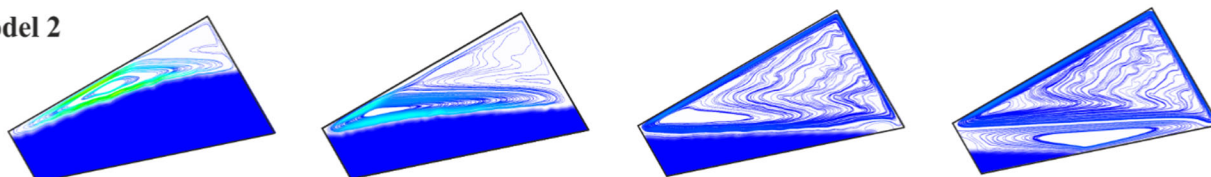
80 min

120 min

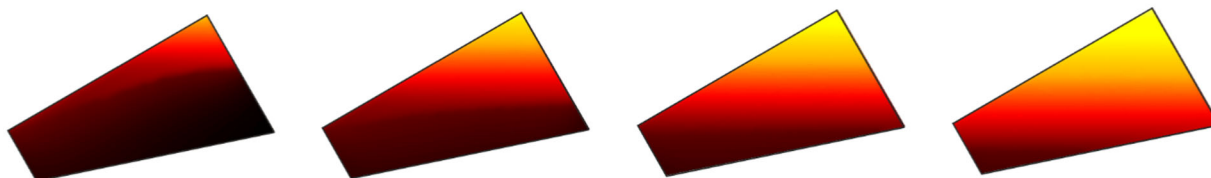
160 min

Model 2

a)



b)



40 min

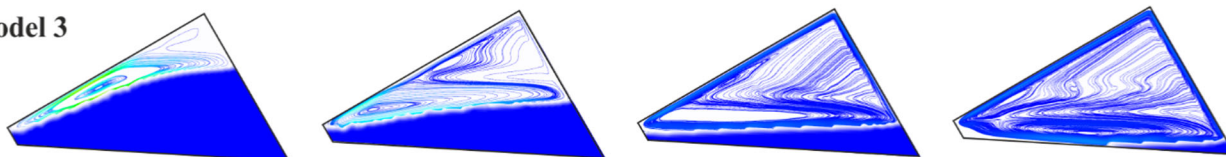
80 min

120 min

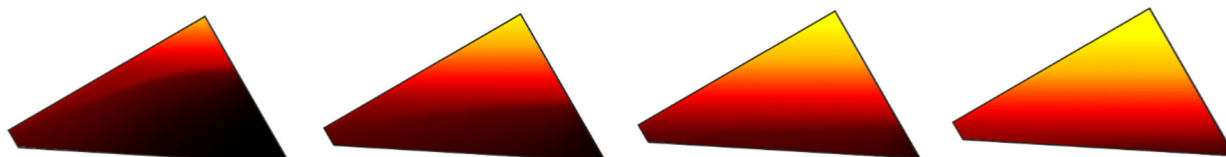
160 min

Model 3

a)



b)



40 min

80 min

120 min

160 min

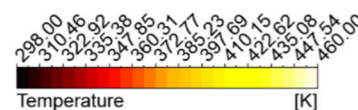
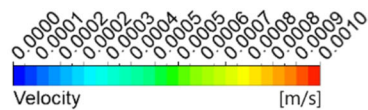
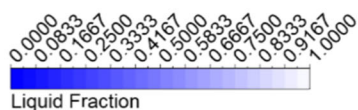


Fig. 9 Time-dependent **a** velocity and liquid fraction (blue color: soli phase, white color: liquid phase, line: velocity streamline) **b** temperature contours for 30° tilt angle ($h_{conv} = 5.8 \text{ W/m}^2\text{K}$, $A_{PCM} = A$)

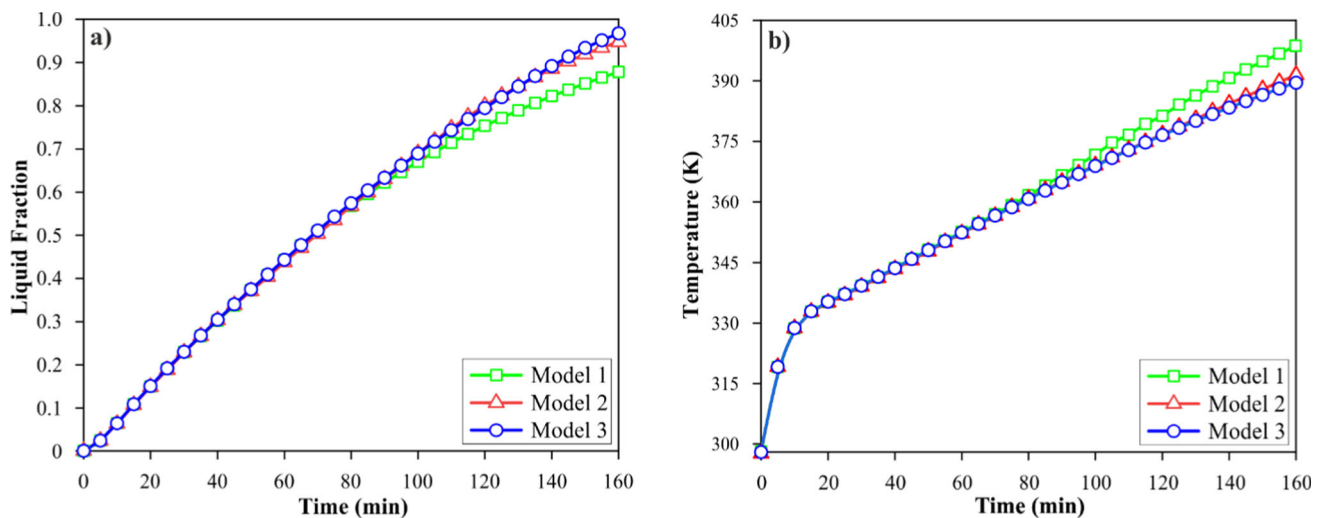


Fig. 10 Time-dependent **a** liquid fractions and **b** top surface average temperature distribution in the melting period all models for 30° tilt angle ($h_{\text{conv}} = 5.8 \text{ W/m}^2\text{K}$, $A_{\text{PCM}} = A$)

angle. These two parameters showed a very close characteristic in the first 100-min period in all models. After 100 min, Model 2 and Model 3 diverged somewhat from Model 1. Numerical data show that Model 3 and Model 2 have very close temperature and liquid fraction values to each other. However, at the end of the melting period, 12% more liquid fraction was obtained in Model 3 compared to Model 1. Due to the reason, the average top surface temperature decreased by 8 K in Model 3.

As can be seen from the velocity vectors and liquid fraction in Fig. 11, since there are more convection effects at 45° than the 30° tilt angle, the temperatures inside the container decreased and the liquid fraction increased. In the range of 40–80 min for Model 1 and at the end of 80 min for Model 2, the right-side surface was disconnected completely from the solid PCM. In addition, a stable melting like a 30° tilt angle occurred in Model 3 and this process took approximately 120 min. Since there was more liquid PCM mass in Model 3 compared to other models during the process, convection effects increased. Almost all the PCM melted at the end of the process.

Figure 12a shows that the liquid fraction increased by an average of 2–3% while the top surface temperature decreased by an average of 8 K for a 45° tilt angle compared to Fig. 8. In the first 80 min, the melting characteristics of all models are almost the same. Afterward, the liquid fraction of Model 2 and Model 3 increased compared to Model 1. Accordingly, at the end of the melting process, 9% and 12% more liquid fractions were observed in Model 2 and Model 3, respectively. As seen in Fig. 12b, depending on liquid fraction, lower temperatures were observed in Model 2 and Model 3 after the 80th minute. At the end of the process, Model 2 and

Model 3 had 12 K and 18 K lower temperatures than Model 1, respectively.

It is understood from Fig. 13 that the highest convection effects in the container were seen at 60° tilt angle. Due to this effect, the lowest temperature values in the container, and the highest liquid fractions were seen. As there is the fastest melting at the 60° tilt angle, all the solid PCM in contact with the right-side surface in Model 1 and Model 2 melted in 80 min. However, in Model 3, still a small amount of solid PCM is in contact with the upper side surface 80th minute. Afterward, in Model 3, melting was faster than in other models and at the end of 160 min, almost all the solid PCM was melted. However, in other models, some solid PCM remained in the container.

As stated above, 60° tilt angle has the highest melting values and lowest surface temperatures as it has the highest convection effects. At this angle, the liquid fraction is 3% and 2% higher and the surface temperatures is 4 K and 6 K lower than the values seen at 30° and 45° tilt angles, respectively. When all three models are compared for a 60° tilt angle, almost all the solid PCM in the container melted in Model 3 at the end of the process, as seen in Fig. 14a. In addition, 89% liquid fraction values for Model 1 and 97% for Model 3 were determined. The lowest average top surface temperature (Fig. 14b) at the end of 160 min was 358 K for Model 3. This value is 5 and 15 K lower than Model 2 and Model 1, respectively.

Figure 15 shows the maximum and minimum temperatures on the PCM container surface and the difference between these temperatures, at the end of processes for different tilt angles of all models. Thus, the variation of the uniformity of the surface temperatures with the use of trapezoidal geometry was determined. When the results are

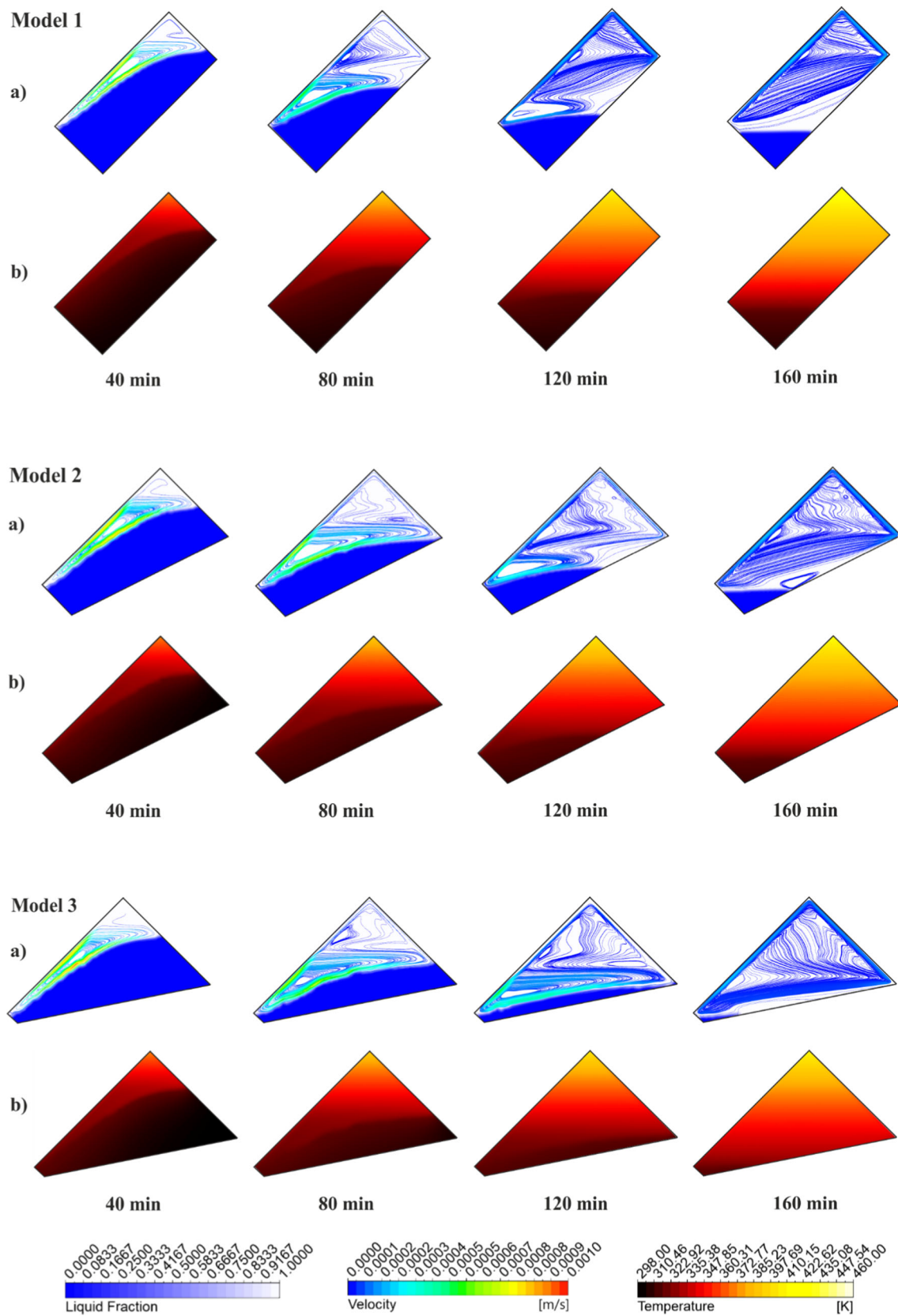


Fig. 11 Time-dependent **a** velocity and liquid fraction (blue color: soli phase, white color: liquid phase, line: velocity streamline) **b** temperature contours for 45° tilt angle ($h_{conv} = 5.8 \text{ W/m}^2\text{K}$, $A_{PCM} = A$)

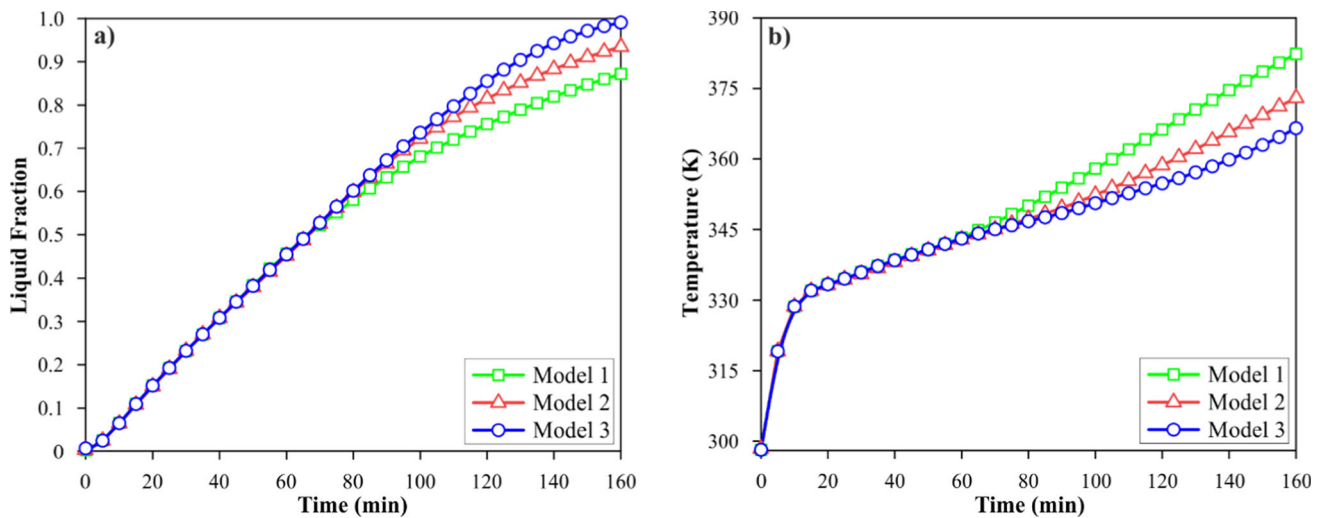


Fig. 12 Time-dependent **a** liquid fractions and **b** top surface average temperature distribution in the melting period all models for 45° tilt angle ($h_{\text{conv}} = 5.8 \text{ W/m}^2\text{K}$, $A_{\text{PCM}} = A$)

examined, the maximum temperature for Model 1 decreased by 32 K with the increase of tilt angle from 30° to 45° , and the maximum temperature decreased by 19 K with an increase from 45° to 60° . However, in Model 2 and Model 3, with the rise of the tilt angle, a more linear decrease in temperature was realized. Accordingly, an increase of 15° in tilt angle for Model 2 decreased the maximum top surface temperature by 21.5 K on average. In Model 3, for every 15° rise, the maximum top surface temperature decreased by an average of 24 K. Just like the highest temperature, container surface minimum temperatures tend to decrease as the tilt angle increases. However, the decreased characteristic is different. For Model 1, with an increase in tilt angle from 30° to 45° , the minimum temperature value decreases by 31.7 K, and with an increase from 45° to 60° , the temperature drop is 8.6 K. For Models 2 and 3, the temperature drops by 25 K as the tilt angle increases from 30° to 45° . Finally, as the tilt angle increased from 45° to 60° , a 5 K decrease was seen for Model 2, but the temperature for Model 3 remained almost unchanged.

Uniformity on the container surface with the use of trapezoidal geometry had a negative effect for 30° tilt angle. However, a positive effect was obtained for 45° and 60° . For 45° tilt angle, Model 2 and Model 3 obtained 3% and 6% more uniform surface temperatures compared to Model 1, respectively, while Model 2 and Model 3 obtained 11.4% and 23% more uniform surface temperatures compared to Model 1 for 60° tilt angle.

Up to this point, the surface cooling performance for different angles and models has been examined. Figure 16 shows the amounts of stored energy. Accordingly, while an increase in the tilt angle slightly increases the amount of latent thermal energy storage in all three models, the total energy

storage amount decreases. The primary factor contributing to this decrease is the higher average temperature at the end of the process despite the reduction in the amount of melting. Additionally, it is observed that the energy storage amounts do not vary significantly among the models with the same angles.

3.3 The Evaluation of PCM Area

It has been mentioned above that trapezoidal geometry positively affects the surface temperature and liquid fraction of the PCM container. It was also found that the best results were seen for the 60° tilt angle and Model 3. From this point of view, another important parameter, the PCM area, was analyzed parametrically in this section. Figures 17, 18, and 19 show velocity, temperature, and liquid fraction contours at 0.8 A, A, and 1.2A, respectively, for a tilt angle of 60° . Model 1, the basic geometry, and Model 3, the trapezoidal geometry, was used for comparison. The results show that more heat can be transferred from the container surface depending on the increase in area, and accordingly, the surface temperatures will decrease. Especially, the use of trapezoidal geometry and the area increase factors are combined, and the right-side surface of the container can be cooled effectively.

Figure 20 shows the time-dependent variation of liquid fraction and average top surface temperatures at different PCM surface areas for Model 1 and Model 3. In Fig. 20a, for Model 3 at 0.8A, at the end of 120 min, all the PCM in the container had melted. In addition, the liquid fraction for Model 1 has been determined as 96%. Model 1 and Model 3 for A have similar liquid fraction values over the first 60 min. However, at the end of the process, it increased to 88% for Model 1 and 98% for Model 3. Finally, for the 1.2A value, a

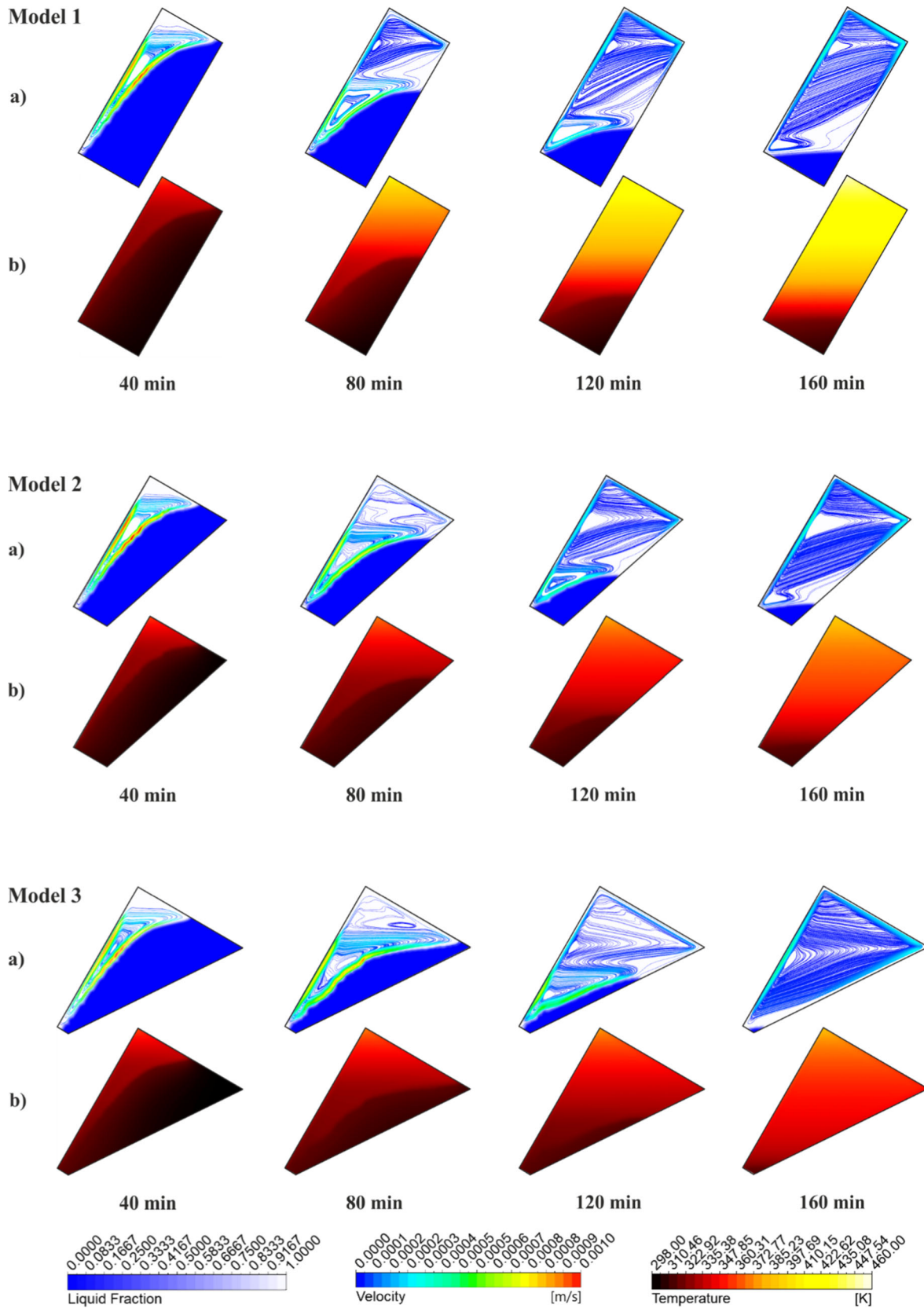


Fig. 13 Time-dependent **a** velocity and liquid fraction (blue color: soli phase, white color: liquid phase, line: velocity streamline) **b** temperature contours for 60° tilt angle ($h_{conv} = 5.8 \text{ W/m}^2\text{K}$, $A_{PCM} = A$)

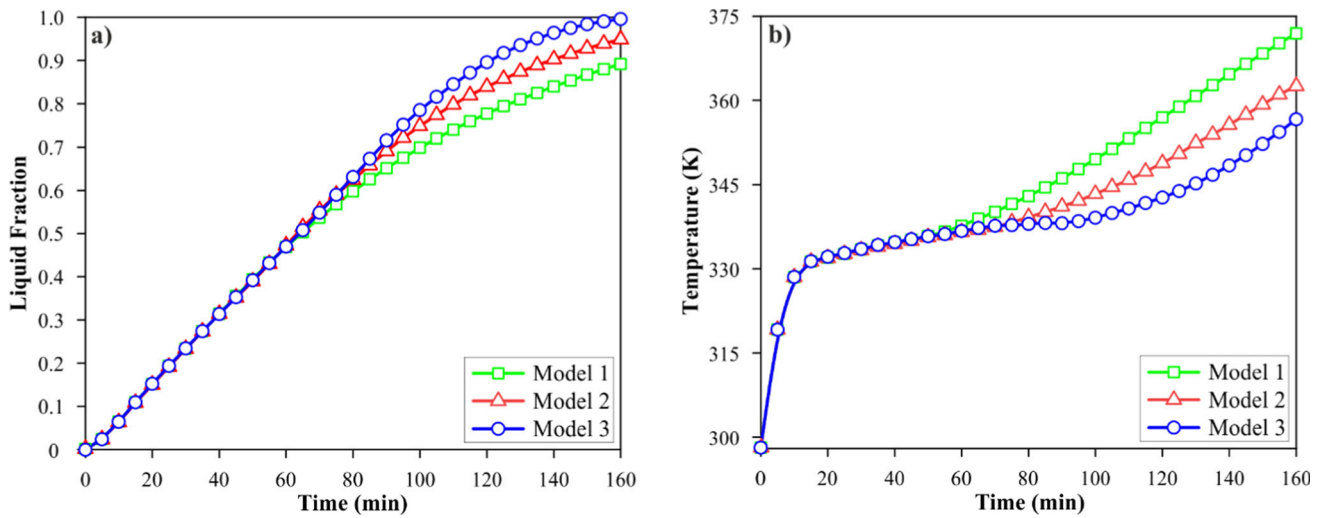


Fig. 14 Time-dependent **a** liquid fractions and **b** top surface average temperature distribution in the melting period all models for 60° tilt angle ($h_{\text{conv}} = 5.8 \text{ W/m}^2\text{K}$, $A_{\text{PCM}} = A$)

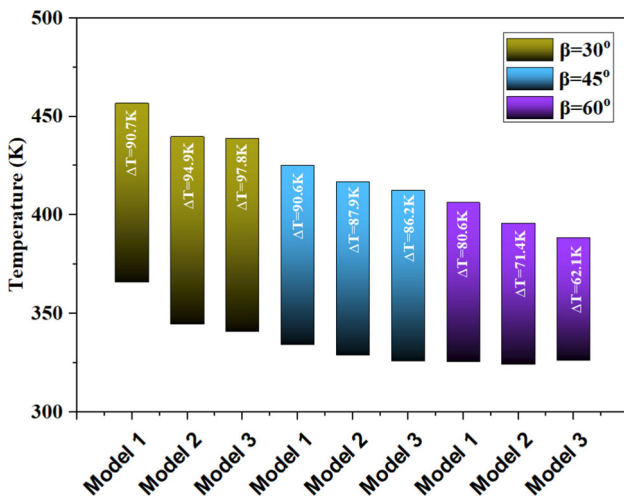


Fig. 15 The highest and lowest temperatures on the PCM container surface for different tilt angle ($h_{\text{conv}} = 5.8 \text{ W/m}^2\text{K}$, $A_{\text{PCM}} = A$)

liquid fraction value of 82% in Model 1 and 89% in Model 3 was determined. When the models are compared among themselves, although an area increase of 0.2 A in Model 1 causes a 6% liquid fraction decrease, Model 3 has a 2% decrease from 1.2A to A and 9% from A to 0.8A.

It is seen in Fig. 20b that the average top surface temperatures decreased due to the increase in PCM area. The results showed that the temperature values were very close in the first 50 min in all PCM areas and models. Afterward, the temperatures were discrete until the end of the melting process. When the temperatures at the end of the process were examined, by reducing the PCM area from 1.2A to A and from A to 0.8A, the temperature increased by 18 K and 3 K, respectively. On the other hand, in Model 3, increasing every 0.2 A PCM area reduced the temperature by about 15 K.

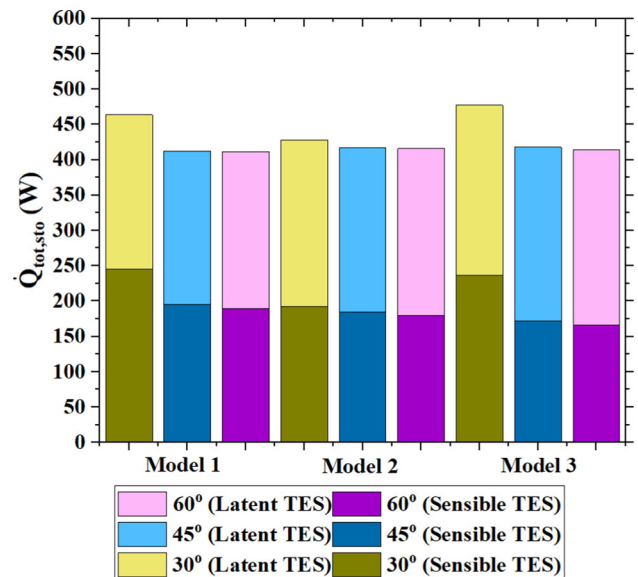


Fig. 16 Energy storage capacities for different tilt angles and models ($h_{\text{conv}} = 5.8 \text{ W/m}^2\text{K}$, $A_{\text{PCM}} = A$)

Figure 21 shows the maximum and minimum temperatures in the PCM container and the differences between these temperatures for Model 1 and Model 3 in different PCM areas. The maximum temperatures inside the container decreased due to the increase in the PCM area. Accordingly, the maximum temperatures are in Model 1; It was obtained as 418 K in 0.8 A, 406 K in A, and 397 K in 1.2 A. This temperature change is almost linear for Model 1. In Model 3, the maximum temperatures were obtained as 401 K, 388 K, and 383 K for 0.8A, A, and 1.2A values, respectively. These results showed that there was no significant decrease in A and 1.2A values. Similarly, the minimum temperature decreased

$$A_{pcm} = 0.8A$$

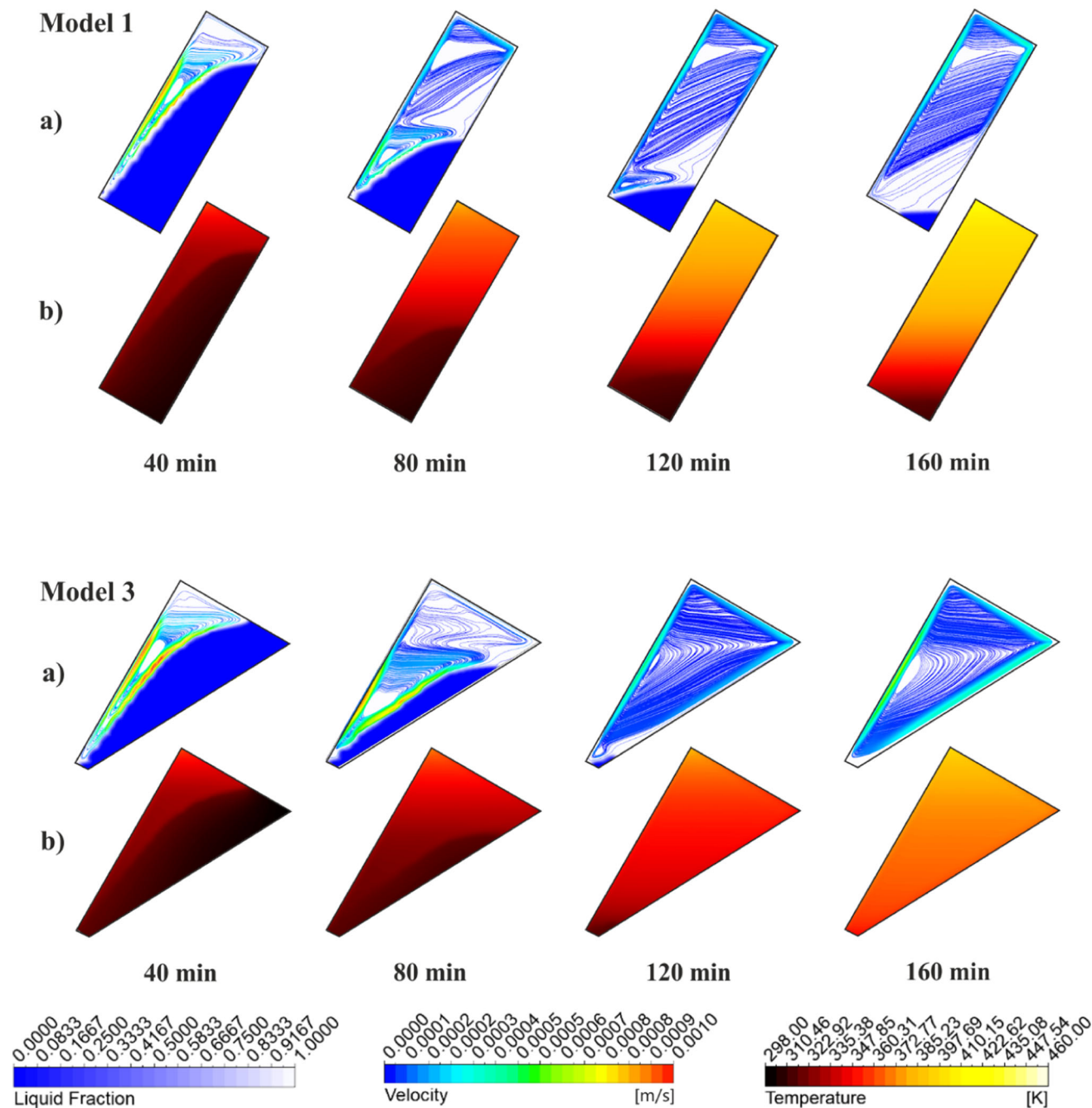


Fig. 17 Time-dependent a velocity and liquid fraction (blue color: soli phase, white color: liquid phase, line: velocity streamline) b temperature contours for $A_{PCM} = 0.8A$ ($h_{conv} = 5.8 \text{ W/m}^2\text{K}$, $\beta = 60^\circ$)

due to the increase in area. However, in both Model 1 and Model 2, the temperature value from A to 1.2A did not change much.

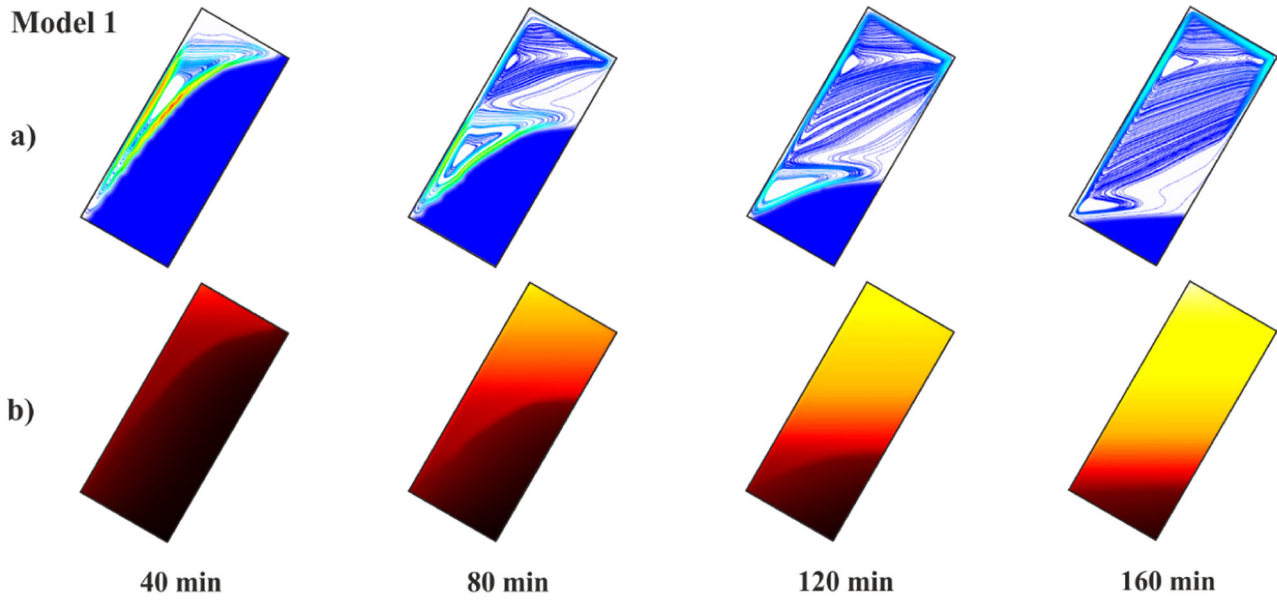
The use of trapezoidal geometry contributed significantly to the uniformity of the surface temperature due to the temperature difference. The results showed that at 0.8A, A, and

1.2A, the surface temperature uniformity increased by 44%, 23%, and 17%.

Figure 22 shows the thermal energy storage capacity as a function of the varying PCM area. The results indicate that the energy storage capacity decreases with an increase in area

$$A_{pcm} = A$$

Model 1



Model 3

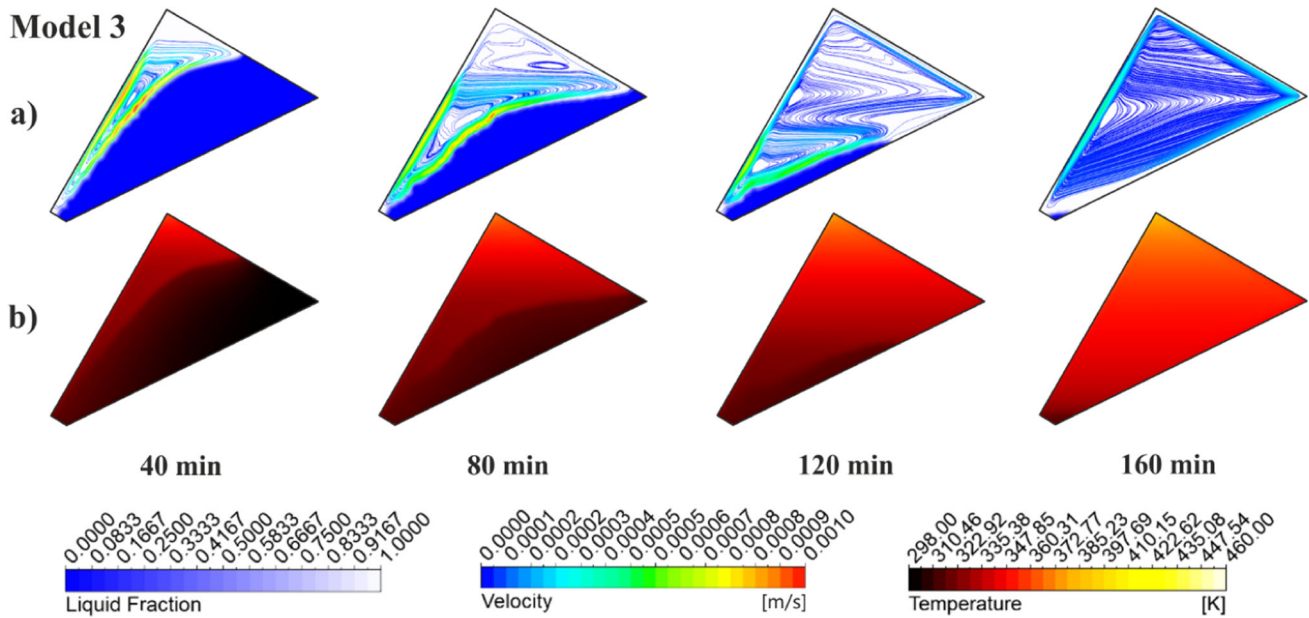


Fig. 18 Time-dependent **a** velocity and liquid fraction (blue color: soli phase, white color: liquid phase, line: velocity streamline) **b** temperature contours for $A_{PCM} = A$ ($h_{conv} = 5.8 \text{ W/m}^2\text{K}$, $\beta = 60^\circ$)

(average 65 W). Additionally, it is observed that the melting amounts are similar for both models at the same area values.

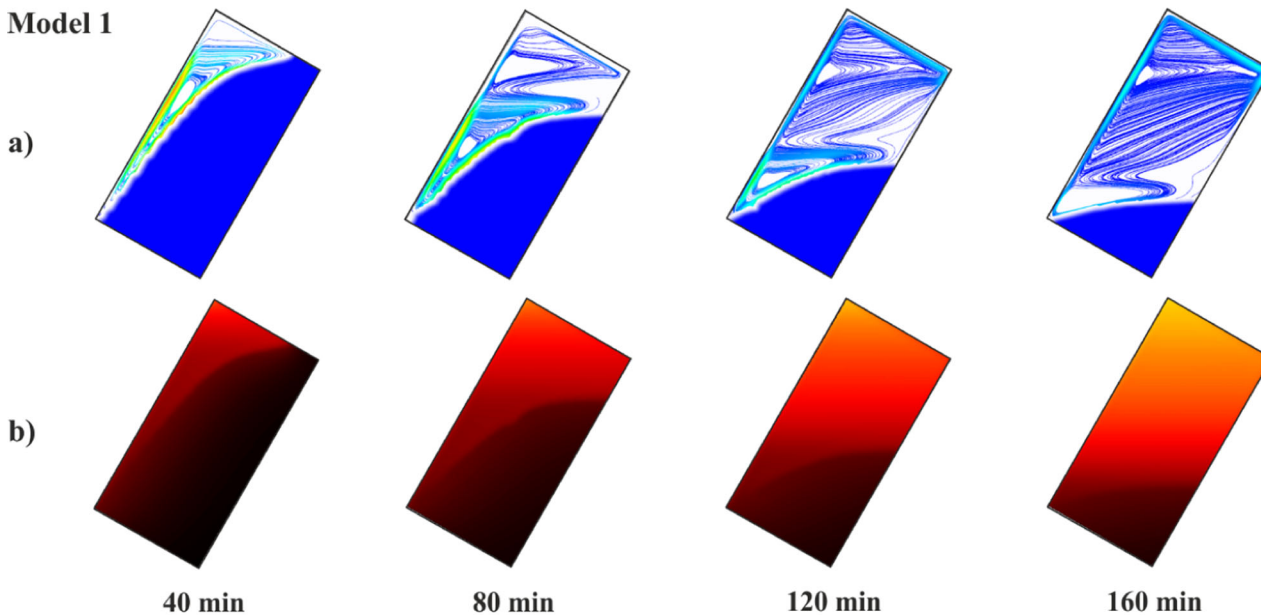
3.4 The Evaluation of Heat Transfer Coefficient

Another important parameter that affects the temperature and melting characteristics of the PCM container is the heat

transfer coefficient. Since the increase in the heat transfer coefficient increased the heat transfer from the side and bottom surface of the container to the environment, the container temperatures decreased, but this caused a decrease in the liquid fraction. In addition, since the heat transfer from the right-side surface of the container (the region where the temperature is maximum) increases with the use of trapezoidal

$$A_{pcm} = 1.2A$$

Model 1



Model 3

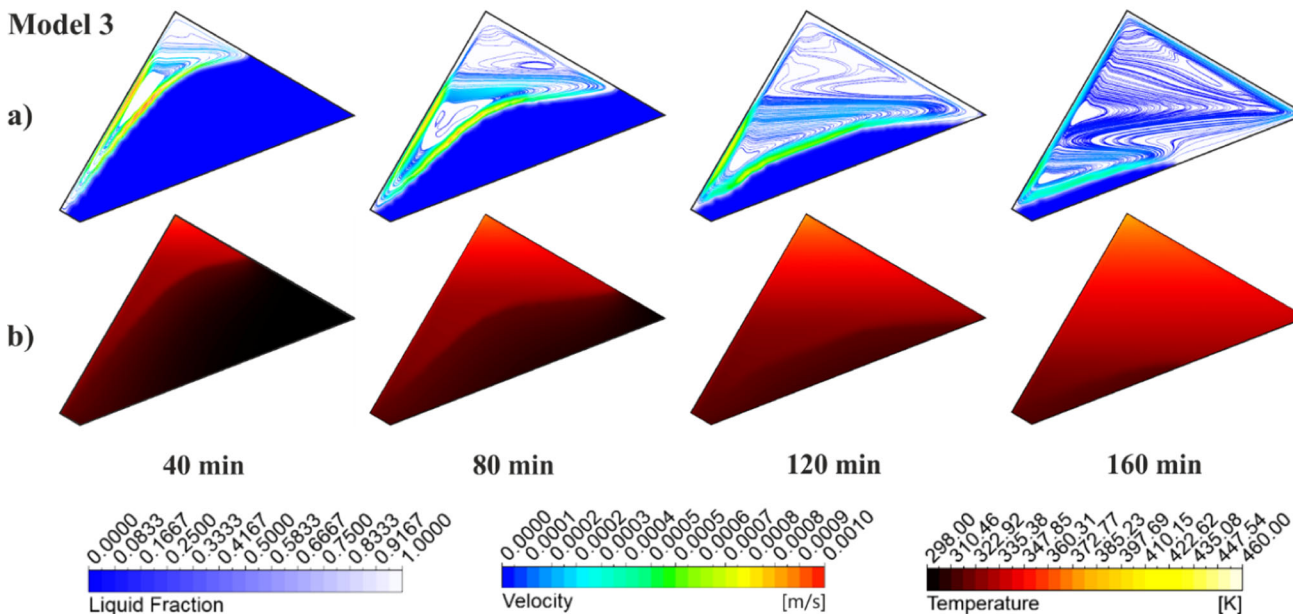


Fig. 19 Time-dependent **a** velocity and liquid fraction (blue color: soli phase, white color: liquid phase, line: velocity streamline) **b** temperature contours for $A_{PCM} = 1.2A$ ($h_{conv} = 5.8 \text{ W/m}^2\text{K}$, $\beta = 60^\circ$)

geometry, it has been observed that the temperature is more uniformly distributed on the bottom surface of the container (Figs. 23,24,25).

Figure 26 shows the liquid fraction and average top surface temperatures of Model 1 and Model 3 at different heat transfer coefficients. In Fig. 26a, the liquid fractions are very

close to each other in almost 80 min for all models and heat transfer coefficients. Moreover, at the end of the melting process, the difference between the values is not much. In Model 1, 89%, 82%, and 81% liquid fraction values were obtained in heat transfer coefficients of 5.8, 8.8, and 11.8 $\text{W/m}^2\text{K}$, respectively. These results showed that there was a 7% and

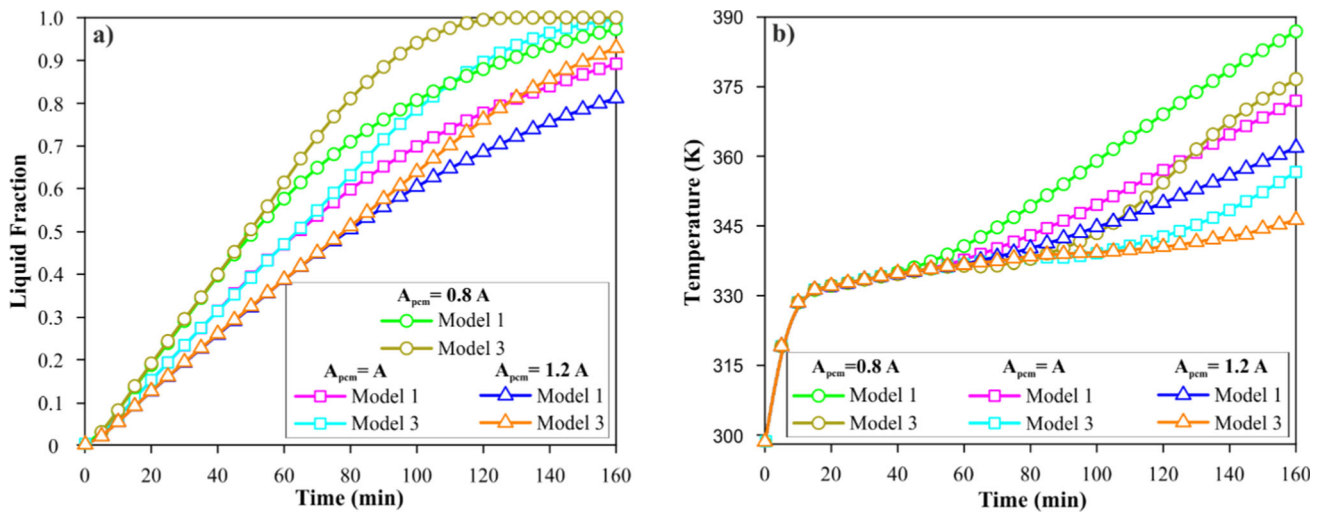


Fig. 20 Time-dependent **a** liquid fractions and **b** top surface average temperature distribution in the melting period all models for different PCM area ($h_{conv} = 5.8 \text{ W/m}^2\text{K}$, $\beta = 60^\circ$)

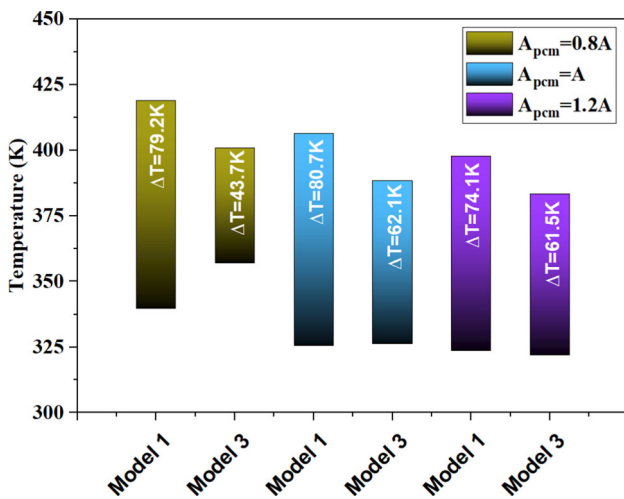


Fig. 21 The highest and lowest temperatures on the PCM container surface for different PCM area ($h_{conv} = 5.8 \text{ W/m}^2\text{K}$, $\beta = 60^\circ$)

1% decrease in the liquid fraction. In Model 3, on the other hand, 4% increases were realized and the heat transfer coefficients of 5.8, 8.8, and $11.8 \text{ W/m}^2\text{K}$ were 100%, 96%, and 92%, respectively. In addition, when Model 3 is compared to Model 1, a 10% increase in the liquid fraction was observed for the $5.8 \text{ W/m}^2\text{K}$ value, 14% for the $8.8 \text{ W/m}^2\text{K}$ value, and 11% for the $11.8 \text{ W/m}^2\text{K}$ value.

Figure 26b shows that the average top surface temperatures for the whole model and the heat transfer coefficients are very close to each other in the first 60 min. At the end of the melting process, temperatures of 372 K, 358 K, and 350 K were obtained for the heat transfer coefficients of 5.8, 8.8, and $11.8 \text{ W/m}^2\text{K}$ in Model 1, respectively. The results showed that with the increase in the heat transfer coefficient, there was a temperature drop of 14 K and 8 K, respectively.

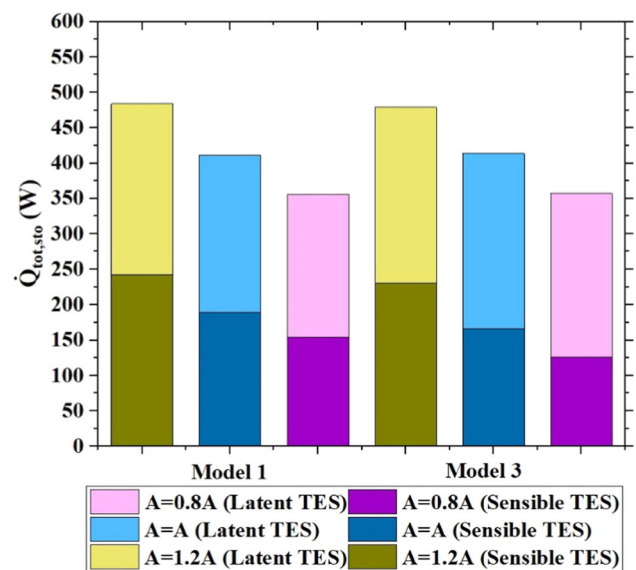


Fig. 22 Variation of energy storage capacity with respect to PCM area ($h_{conv} = 5.8 \text{ W/m}^2\text{K}$, $\beta = 60^\circ$)

In Model 3, temperatures of 355 K, 345 K and 335 K were obtained for the 5.8, 8.8, and $11.8 \text{ W/m}^2\text{K}$ heat transfer coefficients, respectively. Here, the increase in the heat transfer coefficient caused a temperature decrease of 10 K. In addition, in Model 3, temperature drops of 17 K, 13 K, and 15 K were observed in the heat transfer coefficients of 5.8, 8.8, and $11.8 \text{ W/m}^2\text{K}$, respectively, compared to Model 1.

Figure 27 shows the maximum and minimum temperatures inside the PCM container and the differences between these temperatures at different heat transfer coefficients. It is determined from the figure that the minimum temperatures

$$h_{conv} = 5.8 \text{ W/m}^2\text{K}$$

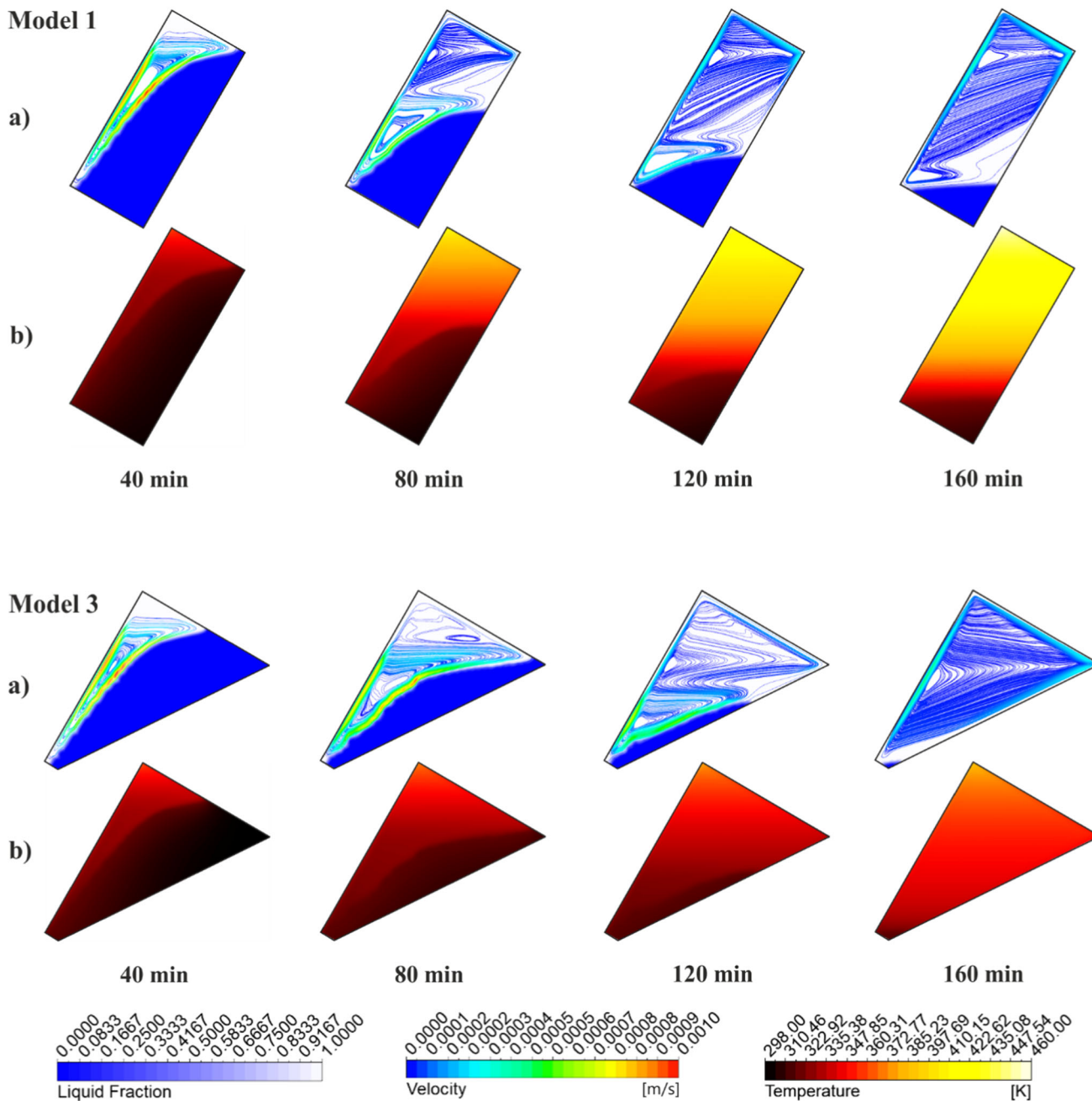


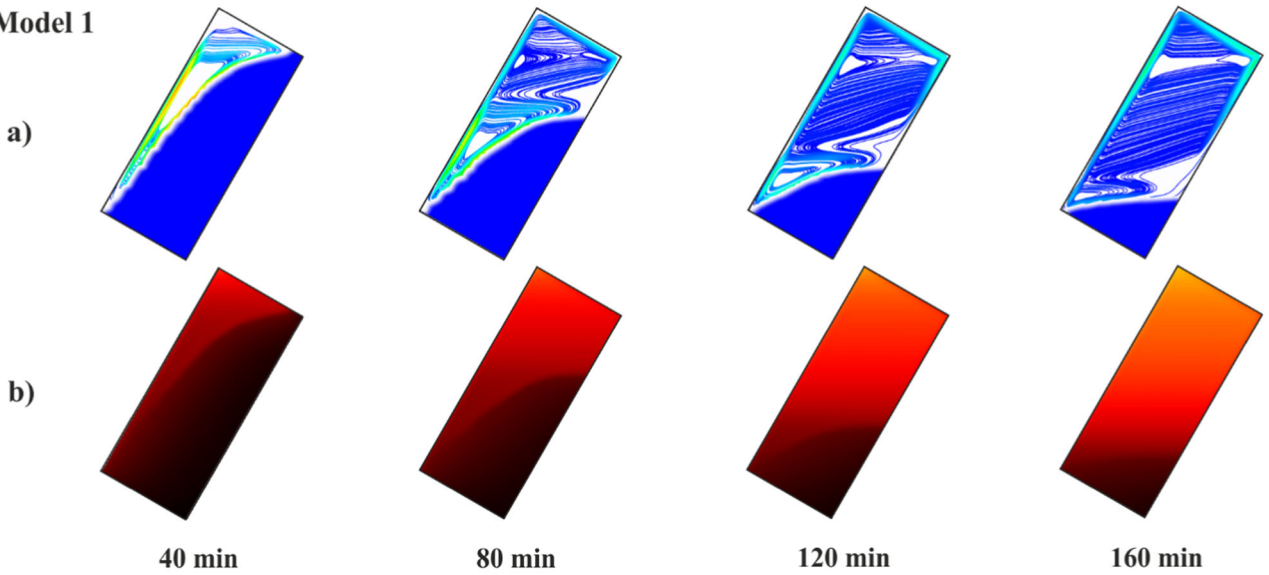
Fig. 23 Time-dependent **a** velocity and liquid fraction (blue color: soli phase, white color: liquid phase, line: velocity streamline) **b** temperature contours for 5.8 W/m²K ($A_{PCM} = A$, $\beta = 60^\circ$)

inside the container are very close to each other for all variables. The maximum temperatures were obtained as 412 K, 388 K, and 358 K in Model 1 at 5.8, 8.8, and 11.8 W/m²K heat transfer coefficients, respectively, and as 388 K, 337 K, and 358 K in Model 3. Accordingly, while 24 K and 13 K drops were observed in Model 1 due to the increase in the heat transfer coefficient, in Model 3, 51 K decrease was observed

with the increase in the heat transfer coefficient from 5.8 to 8.8 W/m²K, and an increase of 21 K with the increase from 8.8 to 11.8 W/m²K. Finally, when the uniformity of the container surface was examined, an improvement of 23% for the heat transfer coefficient of 5.8 W/m²K, 44% for 8.8 W/m²K, and 22% for 11.8 W/m²K was found by using the trapezoidal geometry.

$$h_{conv} = 8.8 \text{ W/m}^2\text{K}$$

Model 1



Model 3

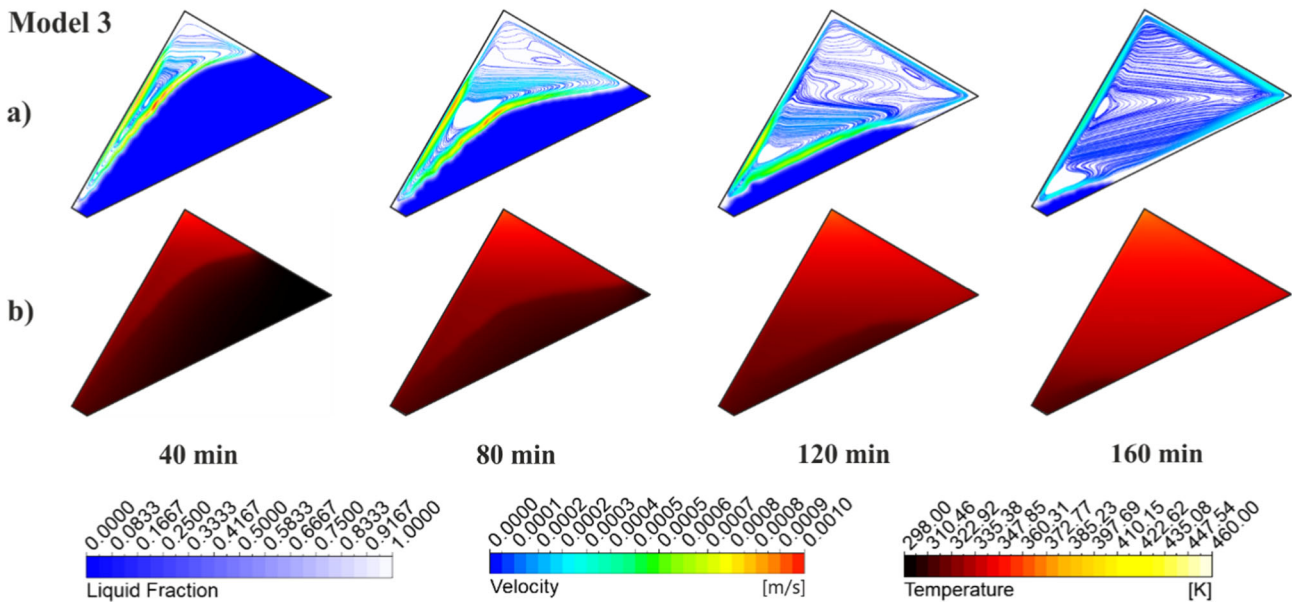


Fig. 24 Time-dependent **a** velocity and liquid fraction (blue color: soli phase, white color: liquid phase, line: velocity streamline) **b** temperature contours for $8.8 \text{ W/m}^2\text{K}$ ($A_{PCM} = A$, $\beta = 60^\circ$)

Finally, Fig. 28 shows the energy storage capacity as a function of the heat transfer coefficient. An increase in the heat transfer coefficient leads to greater cooling within the container, resulting in a decrease in energy storage capacity (average 35W). Additionally, the change in the model does not significantly affect the storage capacity for the same heat transfer coefficients.

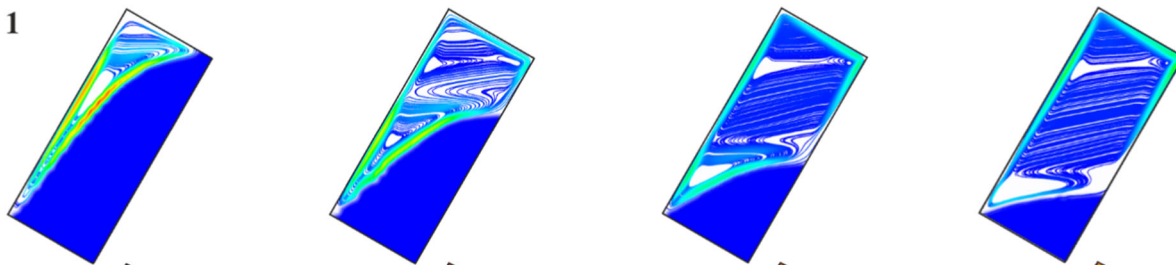
4 Conclusion

In this study, a numerical study was carried out to increase the amount of molten PCM in the container by using a trapezoidal PCM container and accordingly to obtain a lower PCM container top surface temperature. Within the scope of the study, tilt angle, w_1/w_2 , PCM area, and heat transfer coefficient were chosen as variable parameters. When the variation

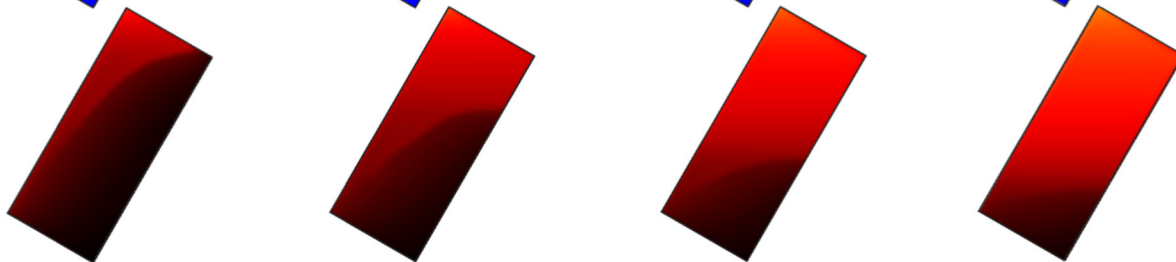
$$h_{conv} = 11.8 \text{ W/m}^2\text{K}$$

Model 1

a)



b)



40 min

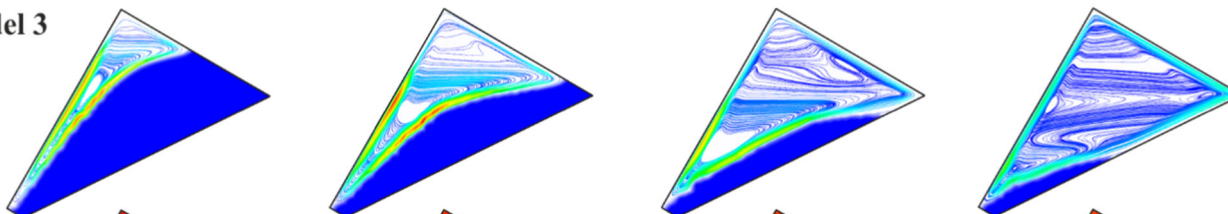
80 min

120 min

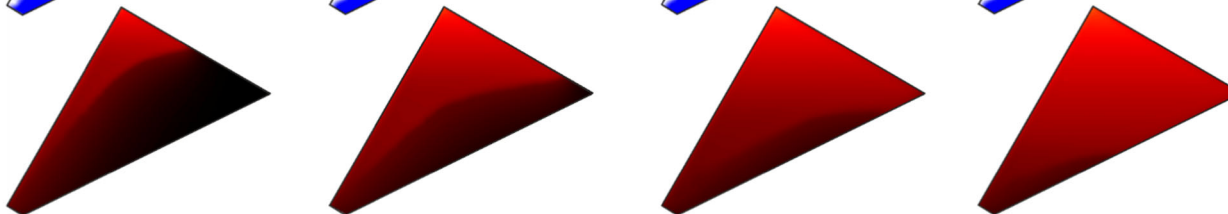
160 min

Model 3

a)



b)



40 min

80 min

120 min

160 min

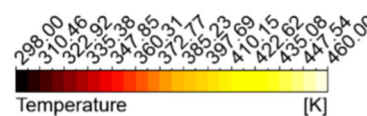
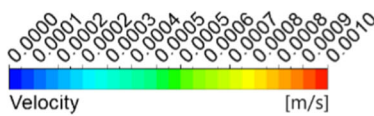
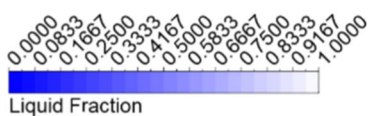


Fig. 25 Time-dependent **a** velocity and liquid fraction (blue color: soli phase, white color: liquid phase, line: velocity streamline) **b** temperature contours for $11.8 \text{ W/m}^2\text{K}$ ($A_{PCM} = A$, $\beta = 60^\circ$)

of the parameters with the proposed geometry was examined, the following findings were obtained.

- The lowest container surface temperature and maximum liquid fraction were observed at 60° tilt angle, where convection reached its highest value.
- It has been observed that with the increase of w_2 length, the hottest part of the container due to convection effects can

be cooled more. In addition, it has been demonstrated that a more uniform temperature distribution on the surface can be achieved by lowering this temperature. Accordingly, for Model 3, where the best results were obtained, at the end of the melting process, the liquid fraction increased by 8%, while the temperature decreased by 15 K. In addition, the surface temperature uniformity increased by 23% in this model.

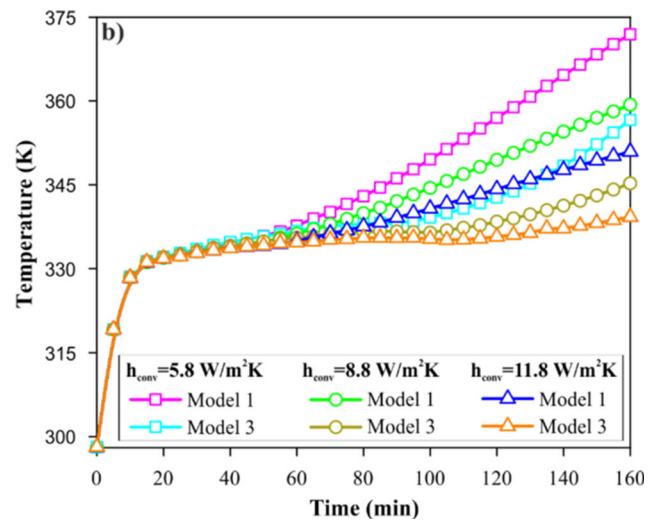
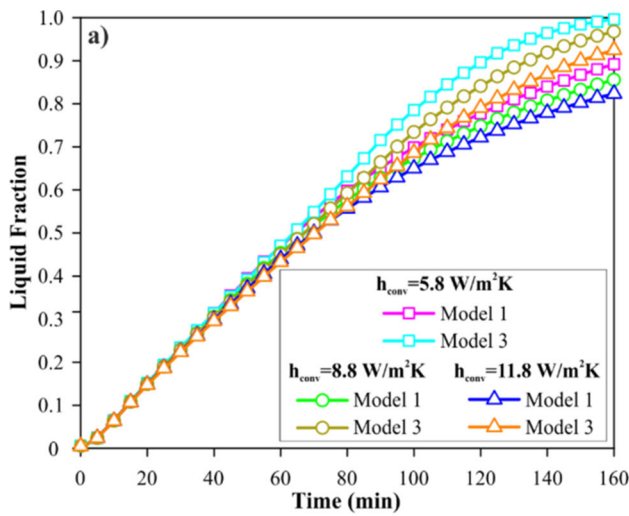


Fig. 26 Time-dependent **a** liquid fractions and **b** top surface average temperature distribution in the melting period all models for different heat transfer coefficient ($A_{PCM} = A, \beta = 60^\circ$)

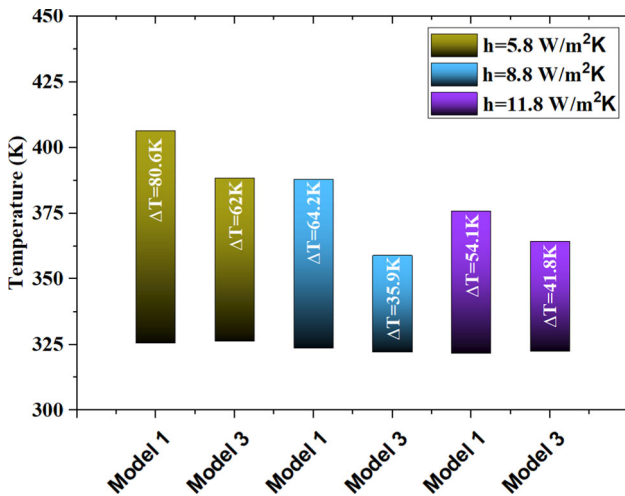


Fig. 27 The maximum and minimum temperatures on the PCM container surface for different heat transfer coefficient ($A_{PCM} = A, \beta = 60^\circ$)

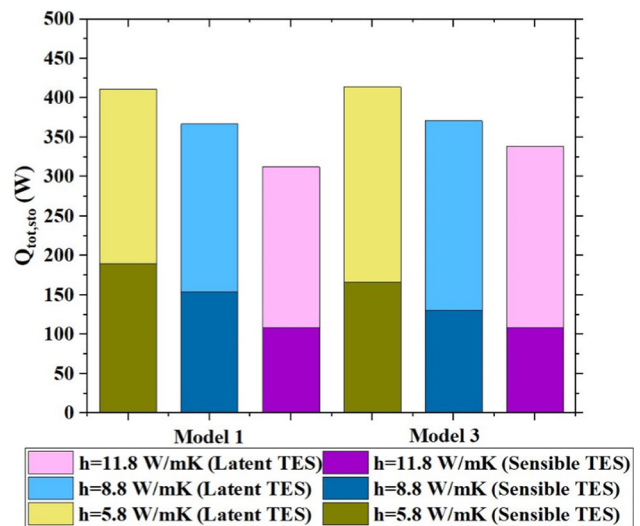


Fig. 28 Variation of energy storage capacity with respect to heat transfer coefficients ($A_{PCM} = A, \beta = 60^\circ$)

- PCM container temperatures drop significantly with increasing PCM area. However, the liquid fraction values decreased accordingly. When analyzed for Model 3, PCM container surface temperature and liquid fraction decreased by 15 K and 11%, respectively. In addition, the uniformity of the container top surface increased by 17%.
- The increase in the heat transfer coefficient, as well as the increase in the PCM area, decreased the surface temperature of the PCM container and the liquid fraction. For the highest heat transfer coefficient of $11.8 \text{ W/m}^2\text{K}$ and Model 3, PCM reduced the container surface temperature and liquid fraction by 20 K and 8%, respectively. Meanwhile, the uniformity of the surface temperature increased by 22%.

- Finally, within the scope of the study, the energy storage capacity was addressed. The results indicate that increases in tilt angle, PCM area, and heat transfer coefficient reduce the energy storage capacity. Additionally, when different models were compared, it was determined that there were no significant changes in energy storage capacity.

With these results, it has been observed that the use of trapezoidal geometry reduces the PCM container surface temperature by increasing the liquid fraction. In addition, more uniform surface temperatures could be obtained with this model. The most important feature of this study is that these positive effects can be obtained by using only a simple geometry change. In future studies, the aim is to analyze

the performance by using different geometries and additional components to increase the heat transfer surfaces in relatively warmer regions of the PV panel surface for better cooling.

References

- Makki, A.; Omer, S.; Sabir, H.: Advancements in hybrid photovoltaic systems for enhanced solar cells performance. *Renew. Sustain. Energy Rev.* **41**, 658–684 (2015)
- Ahmed, M.; Radwan, A.: Performance evaluation of new modified low-concentrator polycrystalline silicon photovoltaic/thermal systems. *Energy Convers. Manage.* **149**, 593–607 (2017)
- Stritih, U.: Increasing the efficiency of PV panel with the use of PCM. *Renewable Energy* **97**, 671–679 (2016)
- Ling, Z., et al.: Review on thermal management systems using phase change materials for electronic components, Li-ion batteries and photovoltaic modules. *Renew. Sustain. Energy Rev.* **31**, 427–438 (2014)
- Ashouri, M.; Hakkaki-Fard, A.: Improving the performance of the finned absorber inclined rooftop solar chimney combined with composite PCM and PV module. *Sol. Energy* **228**, 562–574 (2021)
- Shakibi, H., et al.: Numerical analysis and optimization of a novel photovoltaic thermal solar unit improved by Nano-PCM as an energy storage media and finned collector. *Renew. Sustain. Energy Rev.* **179**, 113230 (2023)
- Abdulmunem, A.R., et al.: Numerical and experimental analysis of the tilt angle's effects on the characteristics of the melting process of PCM-based as PV cell's backside heat sink. *Renew. Energy* **173**, 520–530 (2021)
- Rashid, F.L., et al.: Review of solidification and melting performance of phase change materials in the presence of magnetic field, rotation, tilt angle, and vibration. *J. Energy Storage* **67**, 107501 (2023)
- Zennouhi, H., et al.: Effect of inclination angle on the melting process of phase change material. *Case Stud. Therm. Eng.* **9**, 47–54 (2017)
- Abdulmunem, A.R., et al.: Experimental and numerical investigations on the effects of different tilt angles on the phase change material melting process in a rectangular container. *J. Energy Storage* **32**, 101914 (2020)
- Liu, D., et al.: Numerical evaluation of convective heat transfer properties of two-dimensional rotating PCM melt in the unilaterally heated rectangular container. *Renew. Energy* **193**, 920–940 (2022)
- Emam, M.; Ahmed, M.: Cooling concentrator photovoltaic systems using various configurations of phase-change material heat sinks. *Energy Convers. Manage.* **158**, 298–314 (2018)
- Duan, J.: The PCM-porous system used to cool the inclined PV panel. *Renew. Energy* **180**, 1315–1332 (2021)
- Manikandan, S., et al.: Numerical simulation of various PCM container configurations for solar dryer application. *J. Energy Storage* **86**, 111294 (2024)
- Iachachene, F., et al.: Melting of phase change materials in a trapezoidal cavity: Orientation and nanoparticles effects. *J. Mol. Liq.* **292**, 110592 (2019)
- Liu, H.-Y., et al.: Comprehensive investigation of a novel latent energy storage unit exhibiting enhanced natural convection. *Int. J. Heat Mass Transf.* **219**, 124911 (2024)
- Hekmat, M.H., et al.: The influence of energy storage container geometry on the melting and solidification of PCM. *Int. Commun. Heat Mass Transf.* **137**, 106237 (2022)
- Punniakodi, B.M.S.; Senthil, R.: A review on container geometry and orientations of phase change materials for solar thermal systems. *J. Energy Storage* **36**, 102452 (2021)
- Sharma, R., et al.: Numerical study for enhancement of solidification of phase change materials using trapezoidal cavity. *Powder Technol.* **268**, 38–47 (2014)
- Moein-Jahromi, M.; Rahmani, S.; Rahmani-Koushkaki, H.: Novel designs for PCM passive heat sink of concentrated photovoltaic cells to enhance the heat transfer rate: presenting 4E analyses. *J. Therm. Anal. Calorim.* **149**(4), 1667–1695 (2024)
- Ahmad, A., et al.: Evaluation of new pcm/pv configurations for electrical energy efficiency improvement through thermal management of pv systems. *Energies* **14**(14), 4130 (2021)
- Brent, A.; Voller, V.R.; Reid, K.: Enthalpy-porosity technique for modeling convection-diffusion phase change: application to the melting of a pure metal. *Num. Heat Transf. Part A Appl.* **13**(3), 297–318 (1988)
- Kadivar, M., et al.: Annulus eccentricity optimisation of a phase-change material (PCM) horizontal double-pipe thermal energy store. *J. Energy Storage* **26**, 101030 (2019)
- Bazai, H., et al.: Numerical study of circular-elliptical double-pipe thermal energy storage systems. *J. Energy Storage* **30**, 101440 (2020)
- Yan, P., et al.: Performance enhancement of phase change materials in triplex-tube latent heat energy storage system using novel fin configurations. *Appl. Energy* **327**, 120064 (2022)
- Kamkari, B.; Amlashi, H.J.: Numerical simulation and experimental verification of constrained melting of phase change material in inclined rectangular enclosures. *Int. Commun. Heat Mass Transfer* **88**, 211–219 (2017)
- Seddegh, S., et al.: Investigation of the effect of geometric and operating parameters on thermal behavior of vertical shell-and-tube latent heat energy storage systems. *Energy* **137**, 69–82 (2017)
- Yang, X.-H.; Tan, S.-C.; Liu, J.: Numerical investigation of the phase change process of low melting point metal. *Int. J. Heat Mass Transf.* **100**, 899–907 (2016)
- Shokouhmand, H.; Kamkari, B.: Experimental investigation on melting heat transfer characteristics of lauric acid in a rectangular thermal storage unit. *Exp. Thermal Fluid Sci.* **50**, 201–212 (2013)
- Kurşun, B.; Balta, M.: Evaluation of the different inner and outer channel geometry combinations for optimum melting and solidification performance in double pipe energy storage with phase change material: a numerical study. *J. Energy Storage* **65**, 107250 (2023)
- Kamkari, B.; Shokouhmand, H.; Bruno, F.: Experimental investigation of the effect of inclination angle on convection-driven melting of phase change material in a rectangular enclosure. *Int. J. Heat Mass Transf.* **72**, 186–200 (2014)

Springer Nature or its licensor (e.g. a society or other partner) holds exclusive rights to this article under a publishing agreement with the author(s) or other rightsholder(s); author self-archiving of the accepted manuscript version of this article is solely governed by the terms of such publishing agreement and applicable law.

